UNIVERSITA' DEGLI STUDI DI PADOVA

Departement of Industrial Engineering DII

Master Of Science in Aerospace Engineering

Windage Correlations for flows in Rotor-Stator Cavities

Thesis advisor:

Prof. Dr. **Ernesto BENINI**

Candidate:

Giovambattista VALENTE

Matr. 1231832

Academic Year 2021/2022

Abstract

In the design phases of the propulsion system, tools based on correlations are often used to meet the needs of design offices on various issues (permeability, exchange coefficients).

These correlations are, in part, the result of experimental studies carried out 40 years ago and need to be updated. Safran Aircraft Engines (SAE) technical management has decided to carry out capitalization, documentation and correlation update work. This internship, which falls within this perspective, focuses on the correlations used for the aerothermal modelling of propulsion systems.

Within the methods and tools department of the direction dedicated to the integration of the propulsion system, the mission is to evaluate the performance of commonly used modelling methods, to establish their limits and to propose solutions for improvement. The final objective is to understand the range of validity of the correlations to cover future needs.

In order to meet the need, a tool based on 2D simulations is developed. This tool is designed on the basis of a parametric geometry, allowing the creation of a CFD design of experiments (DOE) whose observables will be compared to the results of the SAE correlations.

Acknowledgement

Abstract

Nelle fasi di progettazione del sistema propulsivo di un aereo, vengono spesso utilizzati strumenti basati su correlazioni per soddisfare le esigenze di progettazione su diverse tematiche (permeabilità, coefficienti di scambio).

Queste correlazioni sono, in parte, il risultato di studi sperimentali effettuati 40 anni fa e necessitano di essere aggiornate. La direzione tecnica di Safran Aircraft Engines (SAE) ha deciso di svolgere lavori di capitalizzazione, documentazione e aggiornamento delle correlazioni. Questo stage, che rientra in questa prospettiva, si concentra sulle correlazioni utilizzate per la modellazione aerotermica dei sistemi propulsivi.

All'interno del dipartimento *Methodes et Outils* della direzione dedicata all'integrazione del sistema propulsivo, la missione è valutare le prestazioni dei metodi di modellizzazione comunemente utilizzati, stabilirne i limiti e proporre soluzioni di miglioramento. L'obiettivo finale è comprendere il range di validità delle correlazioni per coprire le esigenze future.

Per raggiungere tale obiettivo, è stato sviluppato un modello basato su simulazioni CFD 2D. Questo modello è progettato sulla base di una geometria parametrica, consentendo la creazione di un *design of experiments* (DOE) i cui risultati verranno confrontati con i risultati delle correlazioni SAE.

Ringraziamenti

Nomenclature

b	Disk radius
C_f	Friction factor
K	Swirl factor
M	Torque
$\dot{m}$	Mass flow rate
p	Pressure
Q	Volumetric flow rate
r	Local radius
r_c	Source region
r_1	Inner cylinder radius
r_2	Outer cylinder radius
s	Axial gap between the disks
s_a	Axial clearance between rotor/stator and shroud
s_r	Radial clearance
t	Temperature
u	Velocity
u_*	Friction velocity
V_θ	Tangential velocity
V_r	Radial velocity
V_z	Axial velocity
x	Linear displacement
z	Axial coordinate

Greek symbols

δ	Boundary layer thickness
ε	Percentage error
θ	Tangential coordinate
μ	Dynamic viscosity
ν	Kinematic viscosity
ρ	Density
τ	Shear stress
τ_θ	Tangential shear stress
ω	Rotational speed

Dimensionless Groups

C_m	Moment Coefficient
C_w	Throughflow Reynolds number
G	Gap ratio
λ_T	Turbulent flow parameter
Re	Reynolds number
Re_a	Axial Reynolds number
Re_θ	Rotational Reynolds number
Ta	Taylor number
y^+	Non-dimensional wall distance

Acronyms

ATAG   Air Transport Action Group

Windage Correlations for Flows in Rotor-Stator Cavities

CFD   Computational Fluid Dynamics

CFL   Courant-Friedrichs-Lewy number

DOE   Design of Experiments

DX   DesignXplorer

LDA   Laser Doppler Anemometry

RSM   Reynolds Stress Model

SST   Shear Stress Transport model

TSF   Time Scale Factor

TUI   Terminal User Interface

Index

List of figures

List of tables

1. Introduction

1.1 Safran Aircraft Engines

The internship took place on the Safran Aircraft Engines site in Villaroche (see Figure 1), 40km south-east of *Paris*, in *Seine et Marne*. Inaugurated in 1947, the site was intended to host the first test facilities for Safran Aircraft Engines. Today, it brings together research and development, assembly and testing activities on an area of more than 100 hectares welcoming around 5,000 people.

Figure 1 Villaroche Safran Aircraft Engines

My internship takes place within the *Technical Department*, and more specifically within the *Propulsion System Design Offices*. This department brings together all the integration and aircraft manufacturing of the engine or propulsion unit (IPPS). It covers the entire product life cycle, from very early preliminary designs to in-service support, and is a key tool for maintaining Safran Aircraft Engines as a complete major engine manufacturer.

It is made up of 8 departments and cross-functional functions (HSE, planning, business assistants, support functions, etc.). The eight departments are shown in Figure 2.

Figure 2 BEs: Propulsion System Design Offices

I worked in the *Thermal, Fluids and External Aggressions* department. This department is made up of various services, which cover all of the following facets:

• External aggressions: ingestion of particles, icing, fire.

• Fluid circulation: air, fuel and lubrication systems.

• Thermomechanical: overall thermal, axial and radial displacements, clearances.

• Methods and tools: physical modelling and software for analysis, feeding into the four previous areas.

For my part, I did my internship in the *Methods & Tools* service.

The department, through its services, carries out the following missions:

• To specify, design, validate and certify the overall behaviour of propulsion systems.

• To participate in architectural choices, lead technological roadmaps, advance state of the art.

• To capitalize on feedback and ensure the progress process.

• To provide support for the production and maintenance of engines in service

1.2 Civil Aicrafts Engines

The world's best-selling civilian engines are produced by Safran in partnership with General Electric within CFM International. In this 50/50 joint company, all activities are shared: design, development, production, sales and support. The two companies, driven by the success of the new LEAP, recently renewed their partnership until 2050.

The new generation of LEAP turbojet engines replaces the CFM family and equips new aircraft (see Figure 3): the Airbus A320neo (entered into service in August 2016), the Boeing 737 MAX (entered into service in May 2017) and the Comac C919 (certified in December 2016).

Figure 3 Leap Engines

This new turbojet offers fuel consumption and CO_2 emissions reduced by 15% compared to the engines of the previous generation.

Safran Aircraft Engines is also a partner (or supplier) of GE for high thrust engines: CF6, GE90 and GP7200.

At the same time, Safran Aircraft Engines is entering the regional aviation market with the SaM146, developed in cooperation with Russian engine manufacturer UEC Saturn and commissioned in 2011 to power the Sukhoi Superjet 100.

Several innovative projects, focused on carbon-free aviation, have been launched in recent years. Different actions have been selected with, for example, the Open Rotor trial campaign in 2017 and the announcement of the RISE (Revolutionary Innovation for Sustainable Engines) program in 2021.

The CFM RISE program aims to reduce fuel consumption and CO_2 emissions by more than 20% compared to the current generation of LEAP engines present on the Airbus A320neo and Boeing 737 MAX.

The renewal of the partnership between Safran Aircraft Engines and General Electric within CFM International also demonstrates a desire to pave the way for more sustainable aviation, in line with the aeronautics sector's commitment to reduce its CO_2 emissions by half by 2050.

Safran Aircraft Engines' range of civil engines is shown in Figure 4.

Figure 4 Civil Aircraft Engines produced by Safran

2. Context of the Thesis

2.1 Introduction

Windage is defined as a force caused by the relative motion between a fluid and an object. Windage occurs due to a fluid (air for this work) passing through a rotor-stator cavity, measured as a retarding torque on the rotor. It is characterised by three loss components: viscous friction (due to shear stresses within the boundary layer on the surface of the rotor or the stator, of the relative velocity between the fluid and both the rotor and stator surfaces), form drag (separation of the air, as it passes over features present within the cavity like bolts, and the resulting wake formation) and pumping losses (the result of the work done by these features in changing the angular momentum of the fluid). For the case of a smooth rotor surface, the term windage will naturally only refer to losses due to viscous friction.
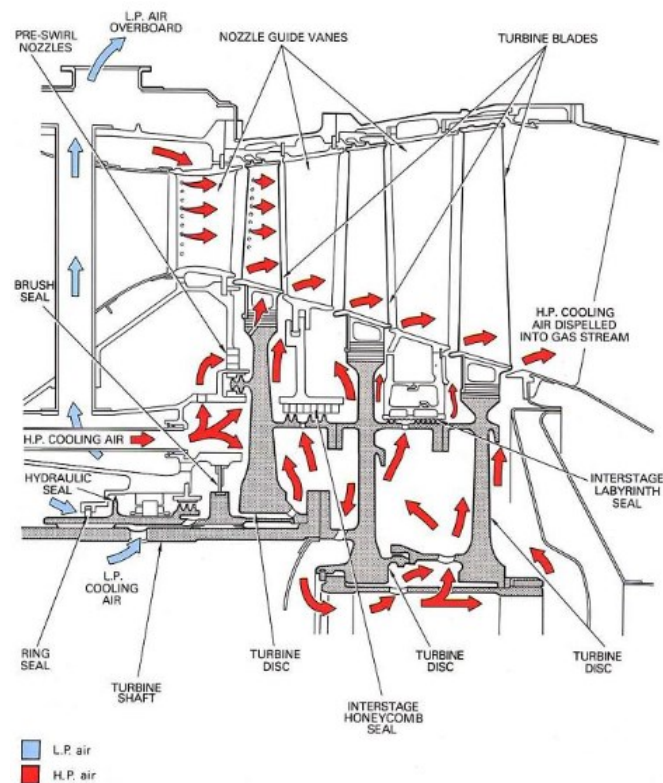
Figure 5 Air path turbine gas engine [1]

Windage losses are for example a big problem in turbine cooling. The figure above shows, for example, the path of the air in a turbine. If we want to increase the specific power output of a gas turbine engine, we need to increase the temperature of the gas flow. Turbine entry temperatures in modern civil engines are currently above 1600°C, too high for the turbine's components to sustain.

An internal air system is therefore used, taking some of the compressor air to cool the turbine discs, blades and nozzle guide vanes. This air generates viscous dissipation as it flows over both rotating and stationary surfaces. This parasitic phenomenon is the so-called windage.

2.2 Thesis structure

This thesis will deal with the study of windage losses in the rotor-stator cavities of civil engines. The strategy chosen to tackle the problem involves the following steps:

- Literature review on rotor-stator systems
- Definition of a CFD tool and validation on experimental data
- Design Of Experiments (DOE) to build the database necessary for the comparison with the results obtained using correlations adopted at Safran Aircraft Engines (SAE)
- Comparison between CFD results and the results given by the correlations.

The third chapter will deal with bibliographic studies, the fourth one with the literature about the academic test cases and the validation of the CFD model. The fifth and sixth chapter will be dedicated to the launch of Design of Experiments (DOE).

Finally, conclusions and futures prospects for these studies will be drawn.

Due to the industrial confidentiality of some information, not all the data used and the results obtained have been included to this report. However, we have always tried to give at least a qualitative description of physic phenomena involved and methodology used, as far as possible.

3. Literature Review

3.1 Dimensionless Parameters

The dimensionless parameters that will be used during the thesis are described below:

- Rotational Reynolds number:

$$Re_\theta = \frac{\rho\omega b^2}{\mu} = \frac{\omega b^2}{\nu} \tag{1}$$

Where b is the disk radius, ρ the fluid density, μ and ν the dynamic and cinematic viscosity and ω the angular velocity of the disk, as shown in the next figure.
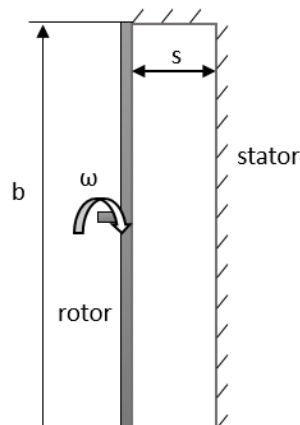
Figure 6 Rotor-stator cavity

The Reynolds number is the ratio of inertial forces to viscous forces within a fluid which is subjected to relative internal movement due to different fluid velocities, this relative movement generates fluid friction, which is a factor in developing turbulent flow. To counteract this effect is the viscosity of the fluid, which tends to inhibit turbulence. The Reynolds number quantifies the relative importance of these two types of forces for given flow conditions. It is used to determine whether a fluid is in laminar or turbulent flow. At low Reynolds numbers, flows tend to be dominated by laminar flow, while at high Reynolds numbers flows tend to be turbulent.

Windage Correlations for Flows in Rotor-Stator Cavities

- Throughflow Reynolds Number

$$C_w = \frac{\dot{m}}{\mu b} \tag{2}$$

Where $\dot{m}$ is the mass flow rate through the system. In this work $C_w > 0$ will mean centrifugal flow and a negative value will imply centripetal flow. To demonstrate the characteristic dimension of C_w, we have to consider the general form of the Reynolds number $Re = \frac{\rho u x}{\mu}$, where u is the flow speed and x the characteristic linear dimension. The mass flow rate can be expressed in the form $\dot{m} = \rho u A$, where A is the area in which the mass flows. If we consider a rotor-stator system with an axial spacing s, the mass flow rate will be:

$$\dot{m} = \rho u 2\pi b s \tag{3}$$

That gives the expression below:

$$C_w = \frac{\rho \dot{m} s}{\mu \rho 2\pi b s} = \frac{\dot{m}}{\mu b} \tag{4}$$

- Turbulent flow parameter

$$\lambda_T = \frac{C_w}{Re_\theta^{0.8}} \tag{5}$$

The turbulent flow parameter provides a measure of the rotationally or radially dominance of the flow. It will be explained in more detail in the next chapters.

- Gap ratio G

$$G = \frac{s}{b} \tag{6}$$

The gap ratio describes the dimensions of the rotor-stator cavity. It is the ratio of the axial spacing to the disk radius b.

- Moment Coefficient C_m

$$C_m = \frac{M}{0.5\rho\omega^2 b^5} = \frac{2\pi \int_0^b \tau_\theta b^2 dr}{0.5\rho\omega^2 b^5} \tag{7}$$

Where M is the moment on one side of the disk and τ_θ is the tangential shear stress. Therefore the moment coefficient depends on the tangential wall shear stress distribution on the disk.

- Swirl ratio K

$$K = \frac{V_\theta}{\omega r} \qquad (8)$$

It is the ratio of the tangential velocity of the core of fluid, to ωr. If $K=1$, we have the same velocity of the rotor wall (rotating wall). If $K=0$, the velocity is the same of the stator wall (stationary wall).

3.2 Flow of a fluid at rest above an infinite rotating disk and of a solid rotating fluid over an infinite fixed disk

In 1905, *Ekman* [2] was the first who studies the flow generated by the rotation of a disk of infinite radius by focusing on the effect of the rotation of the earth on marine currents. In particular he worked on the boundary layer close to the rotating disk which now bears his name.

Von Karman [3] lays the foundations of the analytical analysis of the problem by proposing a solution of the Navier-Stokes equations in the same case as *Ekman* of an infinite rotating disk in a fluid at rest. He then makes the assumptions of a laminar, axisymmetric and stationary flow. It also assumes that the axial velocity does not depend on the radial distance from the axis. In the configuration of the rotating disc of infinite radius in a fluid at rest, a thin layer of fluid is rotated by viscosity, a particle from this boundary layer is expelled by spiralling under the action of centrifugal and Coriolis forces.

We can now consider a disk of radius, b, rotating at a speed ω, in an initially stationary fluid of density ρ, and dynamic viscosity μ. This simple case is referred to as "free disk". Figure 7 illustrates this solution. The phenomenon of "Ekman pumping" is then highlighted: a particle in the *Ekman* boundary layer is expelled in a spiral under the action of centrifugal

and Coriolis forces. This radial flow therefore sucks the particles axially towards the rotating disk [4].
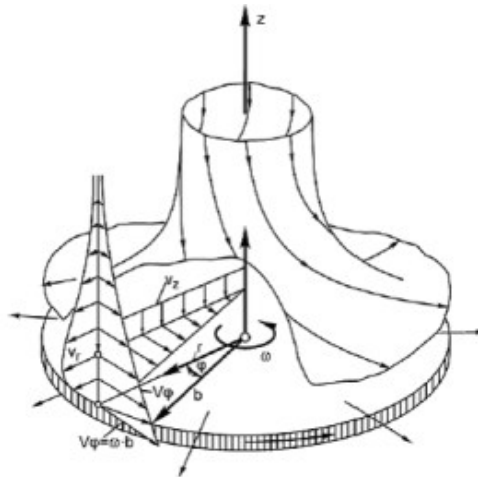
Figure 7 Fluid at rest above an infinite rotating disk

Assuming that the fluid is incompressible and isothermal, *Von Karman* simplified the equations of motion to a set of ordinary differential equations. He also provided solutions to these equations both for laminar and turbulent flows. For the turbulent flow, he used the momentum integral method and the 1/7th power law velocity profile for both the radial and tangential velocities to calculate the moment coefficient and the throughflow Reynolds number C_w.

In 1940, *Bödewadt* [5] extended the analysis to the "opposite" case of a solid rotating fluid above an infinite fixed disk. The boundary layer developing on the disk now bears his name. Figure 8 illustrates this solution. Contrary to the free disk case, the boundary layer close to the disk was found to have a radial inward flow, which produces axial flow pumping outside the boundary layer due to conservation of mass. The thickness of this boundary layer is greater than the free disk boundary layer because the axial outflow tends to thicken the boundary layer while the axial inflow in the free disk case suppresses the boundary layer. As the tangential velocity of the particles decreases near the fixed disk, the centrifugal force no longer compensates the pressure force and the particles are attracted towards the center. In this configuration, the centrifugal force is exactly compensated by the radial pressure gradient, so the rigidly rotating particles away from the disk are in equilibrium. Approaching the disk, the tangential speed therefore decreases the centrifugal force as well. The fluid is then driven in a centripetal and spiral radial motion by the action of the Coriolis force. This centripetal radial flow then expels the particles axially out of the Bödewadt boundary layer.
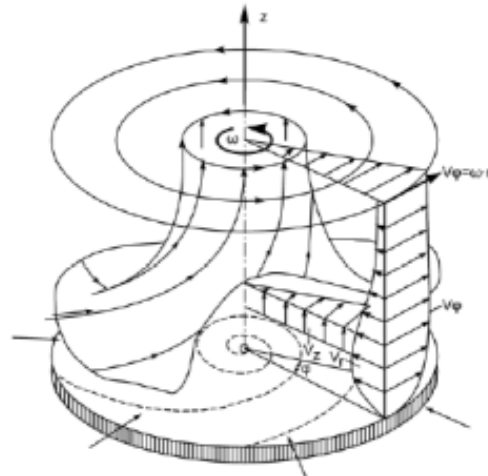
Figure 8 Solid rotating fluid over an infinite fixed disk

3.3 Rotor-Stator cavities

Rotor-stator cavities describe a variety of different configurations of rotating and stationary disks [4]. The basic rotor-stator configuration comprises a rotating disk adjacent to a stationary one. The axial gap, s, represents the distance between the two disks. The rotor-stator system can be extended to different configurations, it can have a stationary or a rotating shroud and an axial or a radial gap (clearance) between shroud and disk, as in Figure 9 (axial clearance s_a)
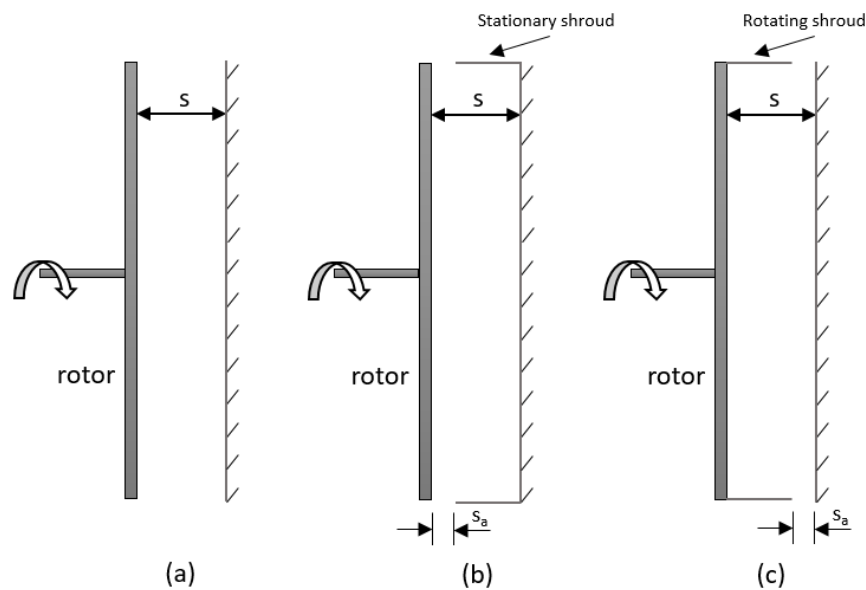
Figure 9 Rotor-Stator Cavity, different configurations

11

Windage Correlations for Flows in Rotor-Stator Cavities

It is helpful to define also some mechanical configurations, different than the rotor-stator systems. Figure 10 shows the co-rotating (a) or contra-rotating disks (b) system.
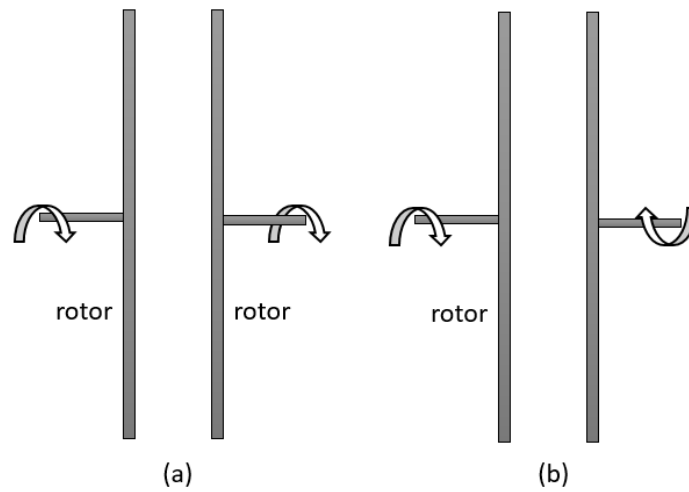
Figure 10 Co-rotating and contra-rotating rotor-rotor cavity

To conclude, Figure 11 shows a rotor-stator system with superimposed radial outflow (a) and superimposed radial inflow (b) (i.e. centrifugal and centripetal flow).
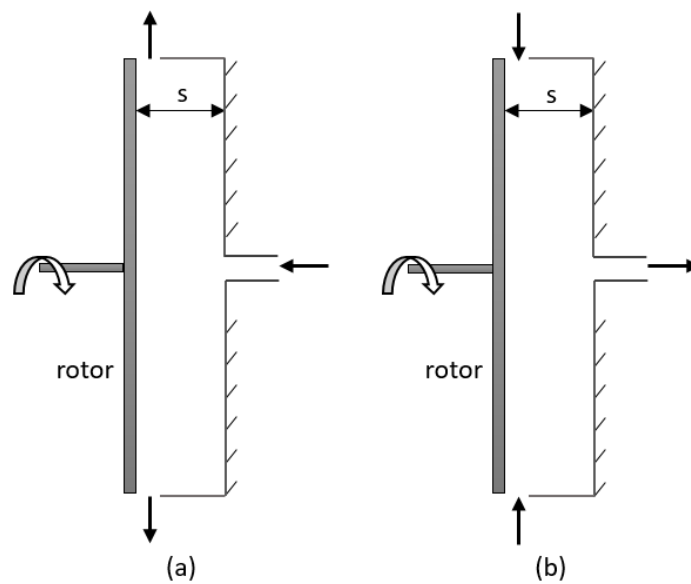
Figure 11 Radial outflow and radial inflow in rotor-stator cavities

3.4 Flow in Rotor-stator cavities

We now consider the case of a flow between an infinite fixed disk (stator) and an infinite rotating disk (rotor), the flow can be characterized by the rotational Reynolds number Re_θ.

In 1950, Batchelor [6] generalized *Von Karman*'s analytical results of Navier-Stokes equations to this type of problem. He then observed that for a large rotational Reynolds number Re_θ, the flow is divided into three regions (Figure 12, left). Two regions of boundary layer with respectively centrifugal radial velocity on the rotor (Ekman layer) and centripetal on the stator (Bödewadt layer). The central region is in solid rotation, i.e. with an almost zero radial velocity and a constant tangential velocity.

Stewartson [7] performed the analysis for small rotational Reynolds number Re_θ, analytically and experimentally, and observed a different topology of the flow: the flow was rotating only close to the rotor. There is no solid rotating zone between the two disks (Figure 12, right).

The Stewartson-type solution becomes unstable from a rotational Reynolds number Re_θ threshold. In both cases, the axial speed is directed from the fixed disk to the rotating disk.
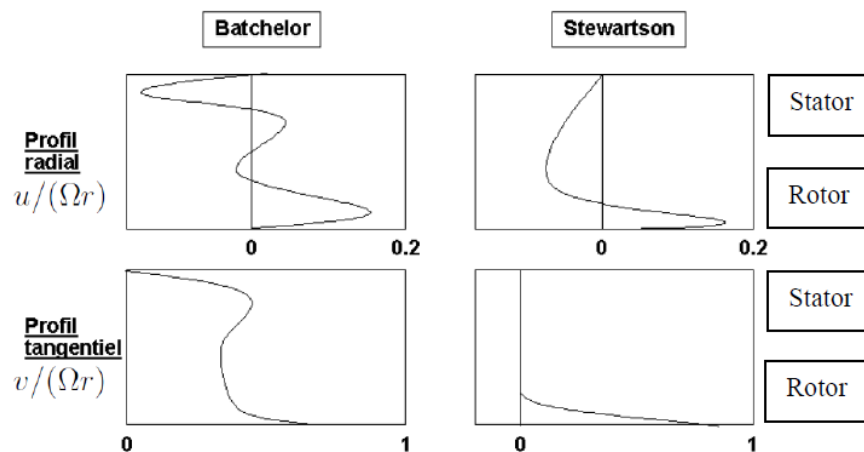
Figure 12 Velocity profiles for Batchelor and Stewartson flows

Daily and Nece [8] performed a theoretical study and experimental measurements to investigate the flow in a shrouded enclosed rotor-stator system (Figure 13), with a constant small radial tip clearance. The disk rotates within a chamber of finite dimensions that is considered to be fully closed so that only a finite volume of fluid is affected by the disk motion. In order to acquire further and systematic information pertinent to this problem,

torque data were obtained over a range of disk Reynolds numbers from 10^3 to 10^7 for axial clearance-disk radius ratios G from 0.0127 to 0.217. Velocity and pressure data were obtained for laminar and turbulent flows. The test rig was filled with either water or four paraffin-base commercial lubricating oils as the working fluid.
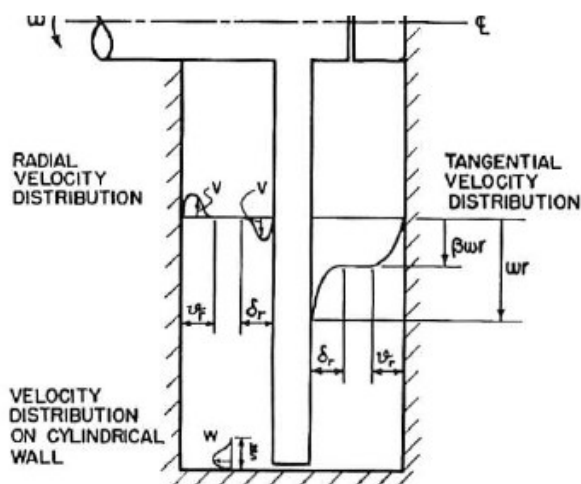
Figure 13 Enclosed cavity (Daily and Nece)

From this study of the fluid mechanics associated with the rotation of a smooth, plane, enclosed disk the following general conclusions were drawn. Four possible modes of flow within the casing exist [8]:

- Regime I: Laminar flow with merged boundary layers (Close Clearance). Boundary layers on the rotor and stator are merged so that a continuous variation in velocity exists across the axial gap s.

- Regime II: Laminar flow with separate boundary layers. The combined thickness of the boundary layers on the rotor and stator is less than the axial gap s. Between the boundary layers is a core region in which no change in velocity is expected to occur.

- Regime III: Turbulent flow with merged boundary layers (Close Clearance). The turbulent counterpart of Regime I, for higher Reynolds numbers and turbulent flow on the circular surfaces.

- Regime IV: Turbulent flow with separate boundary layers.

Regime I exists for all spacings s if the Reynolds number is made sufficiently small. For a small G, Regime II may never exist and for a large G, Regime III may never exist. Regime

IV exists for all G only if the Reynolds number is sufficiently high, if G increases, the transition to Regime IV occurs at a lower Reynolds numbers.

The flow is turbulent for $Re_\theta > 10^5$ and for turbulent flow, G is considered to be large when $G > 0.04$. *Daily and Nece* measured the disk frictional torque at different rotational Reynolds numbers to find the moment coefficient for each flow regime [8]:

- Regime I :
$$C_m = \frac{2\pi}{G\, Re_\theta} \tag{9}$$

- Regime II :
$$C_m = \frac{0.08}{G^{0.167} Re_\theta^{0.25}} \tag{10}$$

- Regime III :
$$C_m = \frac{3.7 G^{0.1}}{Re_\theta^{0.5}} \tag{11}$$

- Regime IV :
$$C_m = \frac{0.102 G^{0.1}}{Re_\theta^{0.2}} \tag{12}$$

Furthermore, summing up the work of *Daily and Nece* and their empirical equations, we can outline these four basic flow regimes mentioned above:
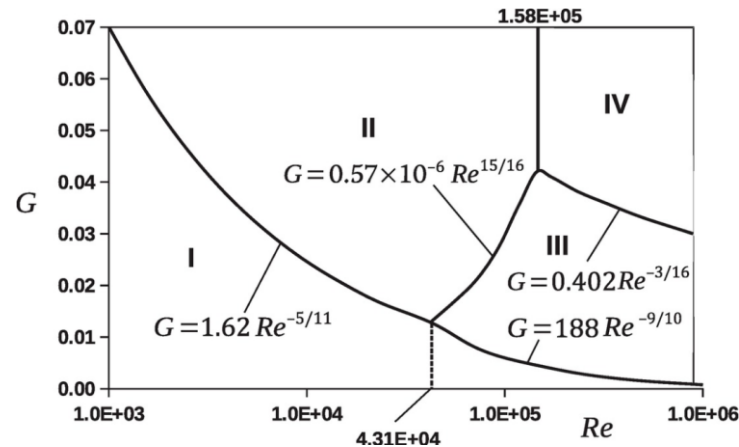
Figure 14 Four Flow regime in an enclosed rotor-stator cavity

The figure 15 below shows torque results for the cavity with the ratio $G=0.115$, the straight lines represent the theoretical expressions, the slope being linked to the regime observed. During this test, the Regime III was not present. Moreover, at the highest Reynolds number, the slope of the torque coefficient tends to decrease. *Daily and Nece* generally obtain a good agreement between their model. The transition between the different regimes is actually gradual (transition starting at the top of the disc and then propagating towards the base).
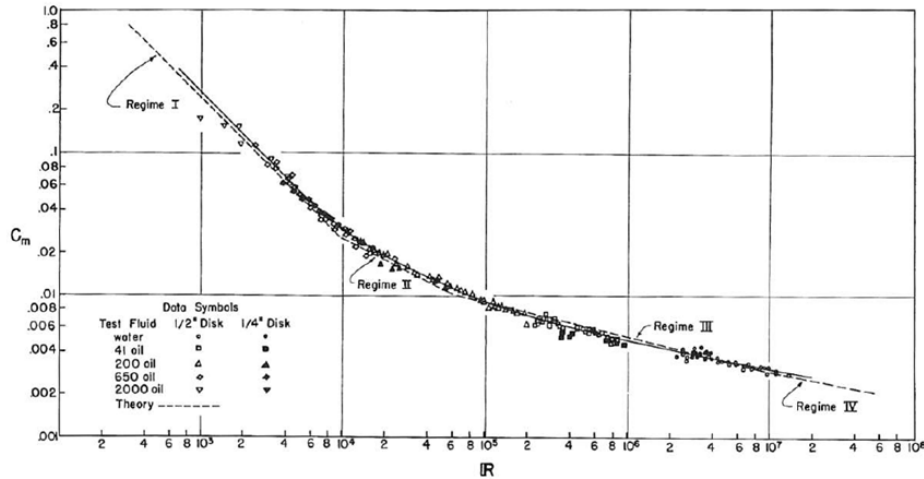
Fig. 11   Smooth-disk torque data: s/a = 0.0255

Figure 15 Smooth disk torque data (Daily and Nece)

Owen [9] performed experiments on rotating disk with a diameter D=0.762 m, rotating at speeds of up to 4500 rev/min, adjacent to a stationary disk, with housing. He measured the moment coefficient and concluded that the disk moment coefficient is strongly dependent on the gap ratio, G.

For the values of $G > 0.12$, it reduces to the free disk values. For $G=0.03$ the value is between the free disc and an enclosed rotor-stator system. He assumed that the tangential velocity was much inferior than ωr so that the non linear inertia forces were neglected in comparison with the Coriolis forces. He solved the Ekman-layer equations using $1/7^{th}$ power law profiles (similarly to von Karman). He found a solution regarding the moment coefficient in a rotor-stator cavity with throughflow, with the dependence on the λ_T parameter in the fourth regime (turbulent) [10].
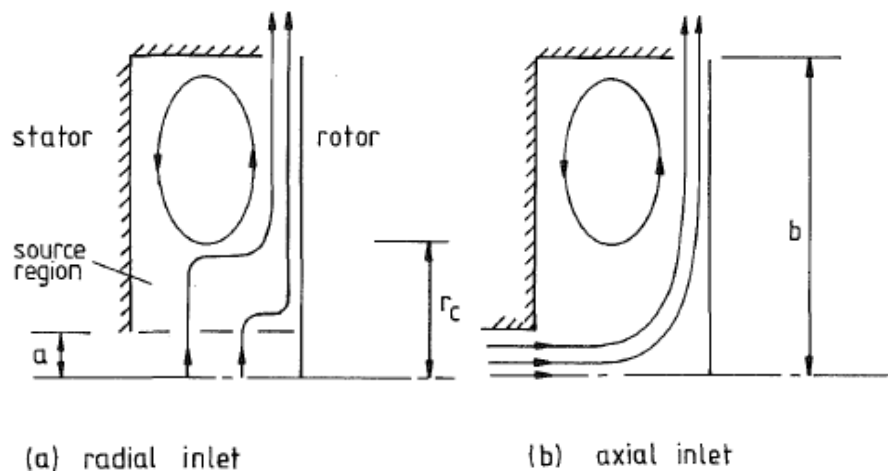
Figure 16 Simplified flow structure in a rotor-stator cavity (Owen)

16

The moment coefficient can be rewritten as:

$$C_m = -4\pi \int_0^1 x^2 \frac{\tau_\theta}{\rho\omega^2 b^2} \, dx \tag{13}$$

The flow has to be considered in two regions: the first one where $x \leq x_c$ in which the relative rotational speed of the core K is zero and the region $x \geq x_c$ in which $K \leq 0$. Starting from x_c, we can define the radius of the source region, described in Figure 16 above. In the figure, $r_c = x_c b$ and $x_c = 1.79\lambda_T^{5/13}$.

In the radial-inlet case (a), flow enters uniformly without swirl at $r = a$ and it is entrained into the boundary layer on the rotor. In the axial-inlet case (b), the flow hits the rotor and moves radially outward. For $r > r_c$, for both flows there is core rotation and a radially inward flow on the stator. At sufficiently low flow rates, it is possible for the axial-inlet case to behave in a similar manner to that of the radial-inlet such that no wall jet is formed and the flow is progressively entrained into the boundary layer.

For $\lambda_T < 0.2$:

$$C_m = Re_\theta^{-0.2}\{0.0729x_c^{4.6} + 0.0389[(1 - x_c^{4.6}) + 14.7\lambda_T(1 - x_c^2) + 90.4\lambda_T^2(1 - x_c^{-0.6})]\} \tag{14}$$

For $\lambda_T > 0.2$:

$$C_m = 0.333 \, \lambda_T \, Re_\theta^{-0.2} \tag{15}$$

Poncet [11] in 2005 contributed to the understanding of "turbulent" flows in the presence of rotation. He proposed, in particular, to study the influence of an imposed flow between a fixed disk and a rotating disk using a test rig with superimpose water as a fluid. Poncet proposed to study these flows according to two axes: experimental study using the Laser Doppler Anenometry (LDA) approach and numerical simulation, with the Reynolds Stress Model (RSM) approach. He used an experimental device to study the turbulent flow, centrifugal or centripetal and with or without fluid pre-rotation. The aspect ratio of the cavity is variable and allows to study the flows with joined or separated boundary layers. Three values of throughflow Reynolds number were tested for radial inflow and radial outflow

Windage Correlations for Flows in Rotor-Stator Cavities

$C_w= \pm1976$, ±5929 and ±9881. Measurements were recorded at two rotational Reynolds numbers, $Re_\theta = 10^6$ and $4,15.10^6$.

Coren [4] in 2007 performed an experimental study on windage effects in rotor-stator cavities with the *Bolt windage Rig* of the University of Sussex. Tests were carried out on a smooth disk with and without mounted protrusions inside an enclosed pressurised housing. The gap ratio was $G = 0.1$, the rotational Reynolds number was $2,5.10^6 \leq Re_\theta \leq 2,5.10^7$ and throughflow Reynolds number was $3.10^4 \leq C_w \leq 1.10^5$. Coren compared the experimental results of the moment coefficient for the rotor-stator system without bolts (plain disk) with the correlations suggested by *Daily et al.*, *Owen* and *Gartner* [12], and found the best match for cases where $\lambda_T < 0.2$ with the model of *Owen*, and for cases where $\lambda_T > 0.2$ with the model of *Gartner*. He used the Laser Doppler Anemometry (LDA) technique to measure the radial and tangential velocities.

Gartner [12] proposed a correlation that takes up some of Owen's bases, and tried to take into account the influence of the stator housing. At low flow rates the correlations were in good agreement, while at high flow rates these correlations tended to overpredict the frictional torque. In the last case, a semi empirical correlation was set to reach good agreement.

Miles [13] worked on the same Bolt windage Rig that was used by *Coren*. A set of plain disk tests as well as tests with rotor and stator-mounted protrusions were carried out under a range of flow conditions that are typical for gas turbine engines and she made comparisons to *Coren*'s tests.

Moghaddam [14] presents a numerical CFD study of the effect of rotor mounted bolts on the moment coefficient and flow structure within a rotor-stator cavity representative of modern gas turbine engine design, using the same *Bolt Windage Rig*. The CFD computations are performed using the commercial code FLUENT. The simulation methodology is first validated using experimental data from plain disk and rotor-stator cavities from the works of *Coren* and *Miles*.

3.5 Co-axial Cylinder with Axial Flow

A turbulent flow can be also confined between two coaxial cylinders, with a rotating cylinder and a stationary one (especially in electrical machines), or two rotating cylinders. An axial throughflow is therefore superimposed. In SAE's turbomachine applications, the rotor-stator cavities can present situations approaching the cylinder case. Some configurations may include two cylindrical rotor walls, co-rotating with different speed or contra-rotating.

One problem facing the design engineer is the optimization of relatively small gaps between concentric rotating cylinders. In most conventional machines, the inner cylinder is the rotor and the outer one is the stator. Type of flow between rotating cylinders depends on the rotation, axial velocity, entrance effect, temperature gradients, and surface conditions [15].

If the flow is a laminar flow, the tangential velocity distribution is linear, whereas the axial flow has a parabolic distribution. If the flow is turbulent, we can have three layers, two viscous layers near the walls and one fully turbulent layer in the middle flow. In the viscous layers, the generation of friction and the energy transfer are influenced mainly by the viscosity of the fluid. An increase of the Reynolds number leads to a decrease of the thickness of the layers.
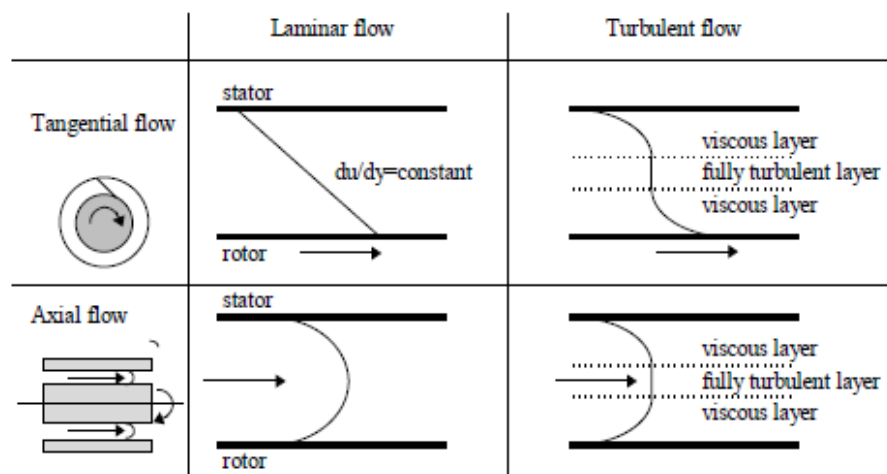
Figure 17 Laminar and turbulent air gap flow (Saari [14])

In these two zones there are the highest velocity gradients. In the middle flow, the chaotic motion of fluid particles is independent of viscosity. In the turbulent axial flow, we have the same regions as in the tangential flow (viscous layer and fully turbulent layer). Because of to the centrifugal force affecting the fluid particles, circular velocity fluctuations appearing in the air gap, called Taylor vortices. The flow can be described by the Reynolds number of

tangential flow $Re_\delta = \frac{\rho V_\theta \delta}{\mu}$ where δ is the air gap length in the radial direction. Furthermore, for an axial flow through the air gap, the Reynolds number becomes $Re_a = \frac{\rho v_m 2\delta}{\mu}$, where v_m is the mean axial fluid velocity. Another parameter to describe Taylor vortices is the Taylor number.

$$T_a = \frac{\rho^2 \omega^2 r \delta^3}{\mu^2} \tag{16}$$

where ω is the angular velocity and r is the radius of the rotor of the cylinder (the rotor radius should be replaced with the mean air-gap radius if the air-gap length is large). The Taylor number is useful if we want to know when Taylor vortices occur. If this number exceeds $1,7.10^3$ the vortices appears (Gazley [16]).
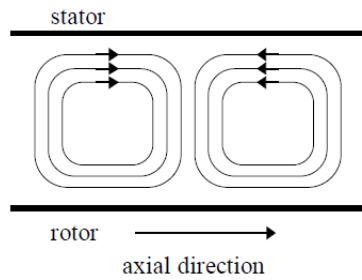
Figure 18 Taylor vortices in co-axial cylinders

The appearance of Taylor vortices is affected by the ratio between the rotor and stator radii, temperature of the rotor and stator and the flow rate of the fluid. The effect of the axial flow is very significant. Four flow regimes have been separated according to Taylor vortices and turbulence of the axial flow, shown in Figure 19: purely laminar, purely turbulent, laminar plus Taylor vortices and turbulent plus Taylor vortices.
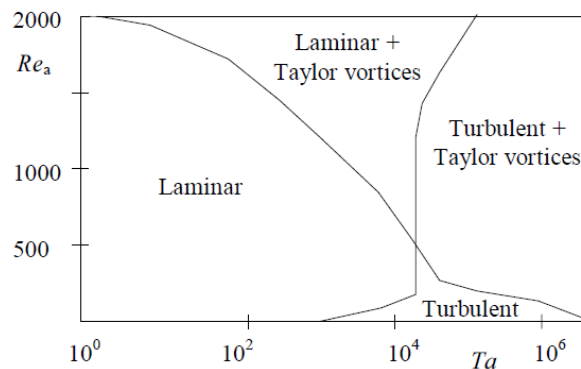
Figure 19 Flow regimes according to Taylor vortices (Saari)

Yamada [17][18] measured the friction torque between concentric cylinders with the inner cylinder rotating, using smooth and circumferentially grooved cylinders in his experiments. Tests were performed with a tangential velocity and an axial flow through the air gap and carried out in water and oil. The highest Couette and axial Reynolds numbers obtained were 6.10^4 and 2.10^4.

The torque was measured in the test section where the velocity field was assumed to be fully developed. Yamada found that:

- When grooves and an axial flow are absent, the friction coefficient increases if the gap between the two cylinders increases. Moreover if the rotational Reynolds number is high, the influence of the gap on the friction coefficient is reduced.
- When the axial flow increases and the value of rotational Reynolds number is small (laminar), the friction coefficient decreases to the theoretical value of the laminar flow. The friction coefficient increases again if the axial flow increases beyond that range (transition to the turbulent flow).
- When the grooves are present on the cylinder, the flow is rarely laminar, the torque hardly decreases if the axial flow increases. If the axial Re is high, the C_f with grooves is larger than that for no grooves. If the axial $Re = 0$ it is barely larger.

When the flow in the annular is without axial flow, the friction factor can be expressed by:

$$C_f = \frac{1}{Re_\theta} \frac{r_2}{r_1} \left(\frac{2}{\frac{r_1}{r_2} + 1} \right) \tag{17}$$

where r_1 and r_2 are the radii of inner and outer cylinder. When the flow is turbulent, Yamada developed the equation below:

$$\frac{1}{\sqrt{C_f}} = 7.54 + 11.5 log_{10} Re_\theta \sqrt{C_f} \tag{18}$$

When the fluid has both tangential and axial velocity:

$$C_f = 0.00759 Re_\theta^{-0.24} \left\{ 1 + \left(\frac{8}{7} \right)^2 \left(\frac{2Re_a}{Re_\theta} \right)^2 \right\} \tag{19}$$

Windage Correlations for Flows in Rotor-Stator Cavities

Bilgen [19] examines the relation of the torque coefficient for the flow between concentric rotating cylinders without axial flow. The flow regimes investigated include laminar, transition and turbulent flow. The inner cylinder is assumed to be rotating and the outer one at rest, the flow is adiabatic and also isothermal. The torque measurements transmitted by the inner cylinder to the fluid are analysed to find the relation for the torque coefficient as a function of dimensionless gap width and Reynolds numbers.

$$C_m = C \left(\frac{s_r}{R_i}\right)^\alpha \left(\frac{\rho \omega R_i s_r}{\mu}\right)^\beta \tag{20}$$

Where R_i is the inner radius, s_r the radial clearance to have the dimensionless gap width s_r/R_i and α, β are empirical exponents.

Saari [15] developed a thermal model for high-speed induction machines and estimates their maximum power. The aim of the study was to calculate the friction and gas-flow losses of a high-speed machine by analytical equations. A special attention was paid on the effect of the surface roughness in the air gap caused by the stator slots.

Also Poncet [20] studied the numerical modelling of fluid flow and heat transfer in a Taylor-Couette[1]-Poiseuille[2] system with axial flow between two differentially heated coaxial cylinders. The system had an inner rotating cylinder and an outer stationary one. In this study, the effects of the rotational speed, the flow rate and the working fluid on the hydrodynamic and thermal fields have been investigated numerically using the Reynolds Stress Model. The results showed that the flow is established quite rapidly. For axial positions larger than 20% of the cavity height, the mean velocity radial profiles and also the Reynolds stresses do not depend any more on the axial position. Turbulence is mainly concentrated in the middle of the clearance between the two cylinders.

He studied the influence of the rotational Reynolds number and Throughflow Reynolds number on the mean tangential and axial velocity for a Prandtl number P_r =0,7. Figures

---

[1] In case of Couette flow, there is not pressure gradient but only relative motion between plates. The profile is linear.
[2] In case of Poiseulle flow, there is not relative motion between plates, the velocity profile is governed by the pressure difference. This profile is parabolic and symmetric about the mid-point.

below show the influence of the rotational Reynolds number and throughflow Reynolds number on the mean tangential and axial velocity (dimensionless).
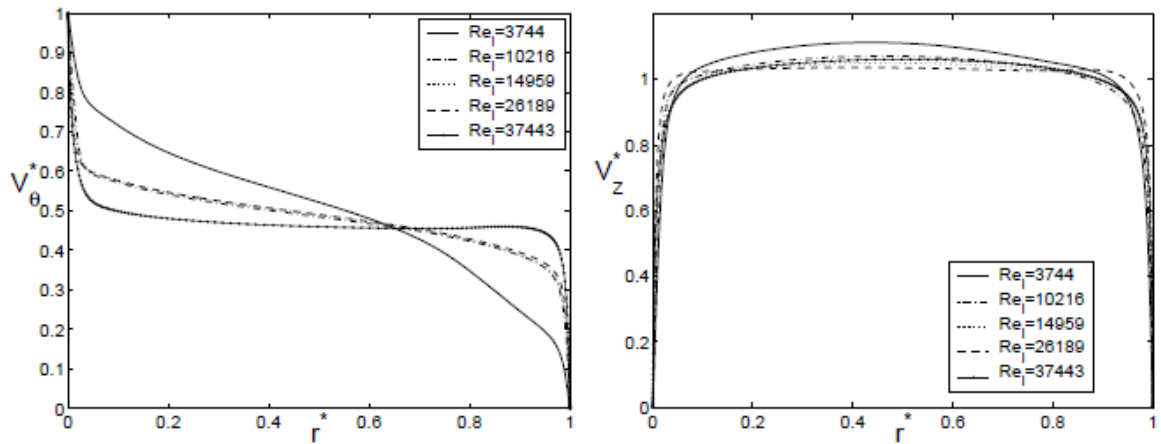
Figure 20 Influence of Reθ on the mean tangential (left) and axial (right) velocity

Regarding the influence of the rotational Reynolds number, Poncet found the same behaviour than that described in figure 17 (right). With a C_w fixed, we see how the mean tangential velocity profile tends to laminar profile in Couette flow for a Re_θ very small, in this case Re_θ=3744. Moreover, if we increase Re_θ, the tangential velocity decreases at mid-radius. As of the mean axial velocity, his distribution is weakly affected by the Reynolds number.
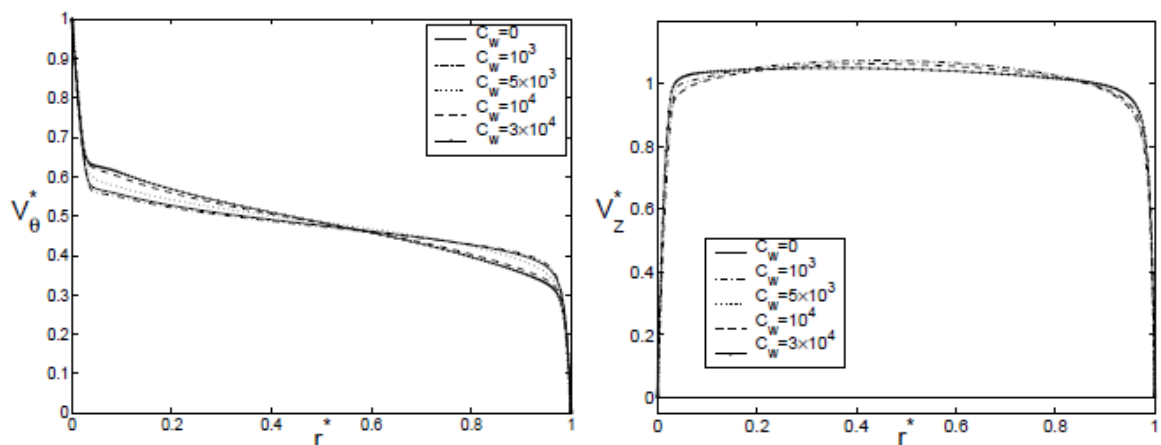
Figure 21 Influence of Cw on the mean tangential (left) and axial (right) velocity

At constant rotational Reynolds number, it can be noticed that the influence of Cw is limited (see figure above).

4. Academic Test Cases

In this chapter we will describe in detail some theses mentioned in chapter 3. These works will serve as a comparison in order to validate a Fluent 2D model, built during the internship at SAE. Once the model has been validated, it will be used, with some attention, to build and launch different DOEs (Design of Experiments).

The first thesis will be the thesis of S.Poncet [11], through which we will be able to compare the velocity profiles for different cases (centrifugal and centripetal flow). In fact, the thesis presents experimental results through LDA (Laser Doppler Anemometry) measurements and a comparison through modelling with the RSM (Reynolds Stress Model) approach.

The results, however, only provide for the radial and tangential velocity profiles in the rotor-stator cavity. Therefore, the Fluent model was built in order to have results consistent with the velocity profiles.

Then we will move on to the three works of the University of Sussex, in particular Coren [4] et Miles [13]. Results will be used to compare the velocity profiles (always with experimental results through LDA measurements) but above all the moments (and moment coefficients), fundamental to define the windage losses, to our modelling results. Therefore, the results of plain disk (disk without protrusions), measured with an inline torquemeter, were used. In plain disk, the windage is due only to the viscous friction due to the surfaces in the cavity.

Finally, Moghaddam [14] will be used to evaluate some velocity profiles and analyze Fluent CFD modelling from University of Sussex.

4.1 Poncet Test Cases

We now place ourselves in the case of an interdisk flow in a confined medium, i.e. of finite radius. This work was taken from Poncet [11], slightly described in the previous chapter.

The end of the disks can be open or closed. Three sub-cases can be considered: closed cavity, open cavity with imposed centrifugal flow and open cavity with imposed centripetal flow. The diagram in Figure 22 represents the cavity, and the test rig.
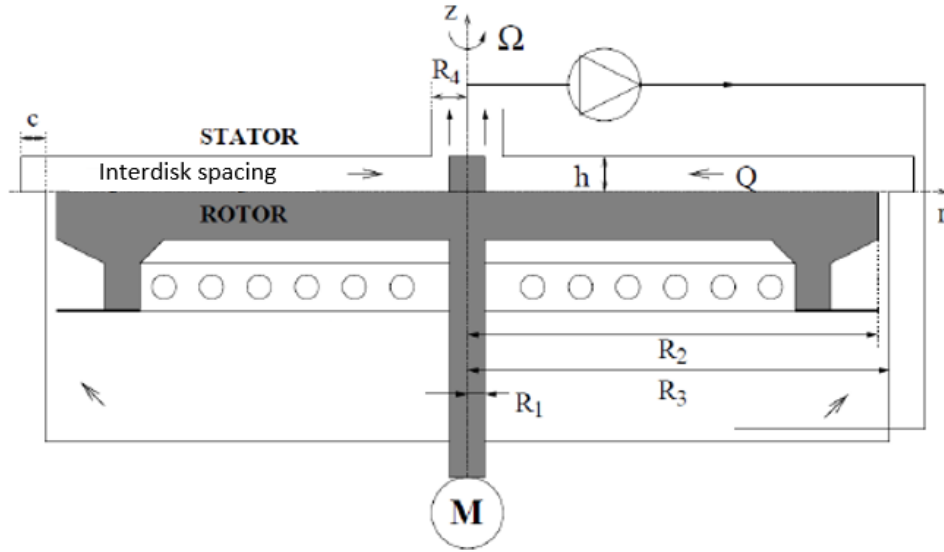
Figure 22 Poncet's Test Rig

In the figure, $h\,(m)$ is the interdisk space, $R_2\,(m)$ the radius of the rotating disk, $\Omega\,(rad/s)$ the rotational speed, $Q\,(m^3/s)$ the volume flow rate of the imposed flux and $v\,(m^2/s)$ the fluid viscosity. We remind that G is the aspect ratio of the cavity, Re_θ the rotational Reynolds number and C_w the rate coefficient of the flux imposed in the cavity. In this work, dimensionless coordinates will often be used as follows:

$$r^* = \frac{r}{R_2}, \quad z^* = \frac{z}{h} \tag{21}$$

It is also common to use the following dimensionless radial distances and velocities.

$$V_r^* = \frac{V_r}{\omega r}, \quad V_\theta^* = \frac{V_\theta}{\omega r}, \quad V_z^* = \frac{V_z}{\omega r} \tag{22}$$

Different types of interdisk flow can be observed depending on the different parameters:

- Flow with joined or separated boundary layers. For G large enough, the boundary layers are separated. For low G, typically G <0.01, the boundary layers are joined and the tangential velocity is linear from stator to rotor.

- Laminar or turbulent flow. For Re_θ large enough, typically Re_θ >10^5, the flow undergoes a laminar/turbulent transition in an enclosed cavity.

- Stewartson type flow (only the rotor boundary layer is entrained) or Batchelor (solid core in rotation).

The cavity corresponds to two smooth disks, a rotating wall (the rotor) and a stationary wall (the stator), in an annular domain. In order to describe generally the geometry, observing the Figure 22, R_1 = 38 mm and R_2 = 250 mm are the inner and outer radii of the rotating disk, and the domain is bounded by two coaxial cylinders. The origin of the z axis is located on the rotating disk.

The rotor and the central hub which is attached to it are in uniform rotation of speed Ω along the z axis. The two radial spaces at the entrance and at the exit of the cavity make it possible to impose a centrifugal or centripetal flow. Finally, the interdisk space h can be variable.

In this case, as $R_2 \approx R_3$ and $R_2 >> R_1$, the aspect ratio G, can be defined as $G = h/R_2$.

Among the various studies Poncet carried out, 6 were chosen to cover a wide range of values for Re_θ, C_W and λ_T.

	Re_ϑ / 10^6	C_w / 10^3	λ_T	G
Case1	1,04	1,9	0,03	0,036
Case2	1,04	5,9	0,09	0,036
Case3	1,04	9,8	0,15	0,036
Case4	4,5	10,3	0,05	0,036
Case5	4,5	10,3	0,05	0,012
Case6	1,04	-5,9	-0.09	0,036

Table 1 Six Poncet's Cases studied with Fluent

Windage Correlations for Flows in Rotor-Stator Cavities

In general, therefore, the range chosen for the 6 cases is the following:

$$1,04.10^6 < Re_\theta < 4,5.10^6$$

$$-5,9.10^3 < C_w < 1,03.10^4$$

$$-0,09 < \lambda_T < 0,15$$

In these six cases, we had the possibility to study three centrifugal cases, two centrifugal cases with the extreme values used by Poncet for Re_θ and C_w and a centripetal case.

The study carried out on ANSYS Fluent includes an influence in the mesh, to see if it is possible to coarsen the mesh without losing efficiency and precision. Moreover, a comparison between the two turbulence models most used for this type of simulations, namely the k-ε realizable and the k-ω SST, was included. Furthermore, a study on the various reference systems was carried out (not integrated in this report), and it was noted that a relative (frame motion in the fluid cell zone conditions) or absolute reference did not have an impact on the results.

Finally the results for the velocity profiles are compared. We will compare the LDA and RSM approach, in order to see the difference both with Poncet's experimental results and his modelization.

Before starting with the definition of our modelization, a short description of Poncet's studies is given in the next paragraphs.

4.1.1 Description of Poncet's studies

Closed cavity

Figure 23 represents the velocity profiles in the base case of adiabatic flow in a closed cavity for r*=0.44-0.56-0.80. The Reynolds number is Re_θ=1,04.10^6 and G= 0.036. As in all other following figures, the solid line represents Poncet's modelling RSM, while the white circles the LDA measurements.

As described in the previous chapter, we can observe the flow of Batchelor type, with the three distinct zones of the flow: a boundary layer centripetal on the stator (Bödewadt layer),

a rotating central core and a boundary layer centrifugal on the rotor (Ekman layer). This means that in the Bödewadt layer, the mean radial velocity is negative and the mean tangential velocity is between 0 and $K\Omega r$. Poncet shows that, approaching the axis of the cavity (in the figure from right to left), the thickness of the Bödewadt boundary layer decreases and the minimum radial velocity increases. The swirl ratio V_θ^* is almost constant close to 0,45.

The Ekman layer is always centrifugal (the average radial speed is positive). As r decreases, the thickness of the Ekman boundary layer decreases and the maximum of the radial velocity in this layer increases.
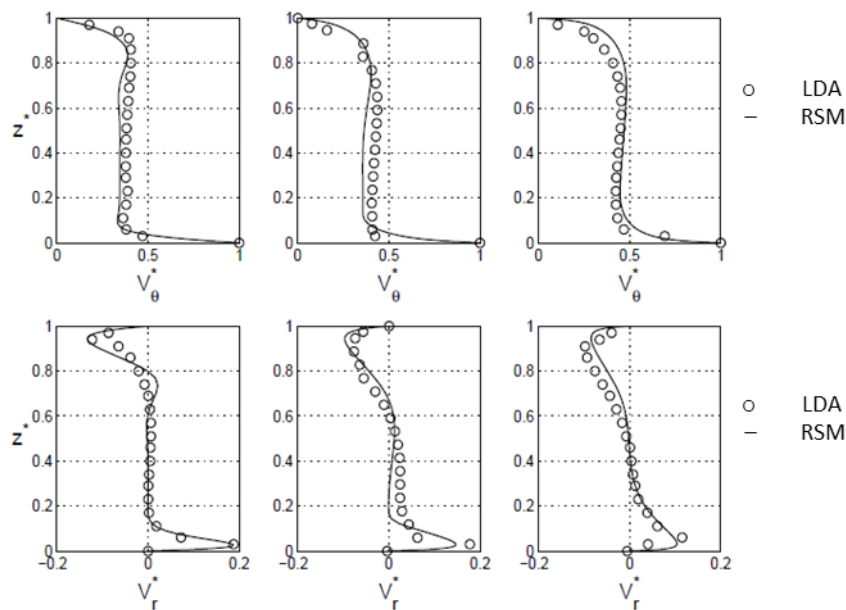
Figure 23 Radial and tangential velocity profiles in a closed cavity, r*=0.44-0.56-0.80

The streamlines below highlight the recirculation of the fluid in the cavity due to the coupled effects of the Ekman (centrifugal) and Bödewadt (centripetal) layers.
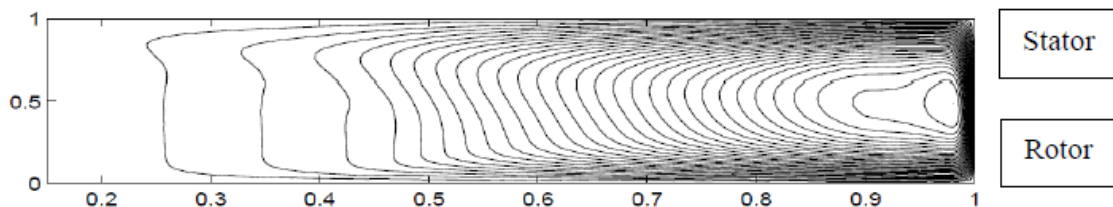
Figure 24 Streamlines in a closed cavity

For a flow with separated boundary layers, Poncet shows that the Reynolds number only moderately affects the structure of the flow, the recirculation zone at the periphery of the cavity decreases [11].

Confined cavity with imposed centripetal flow

Figure 25 shows the velocity profiles for the same three radii in the case of a cavity with centripetal flow. The dimensionless parameters are: $Re_\theta = 1,04.10^6$, $C_w = -5929$ and $G = 0.036$ (i.e. 9 mm). Far from the axis, so $r* = 0.80$ the flow resembles a closed cavity flow of the Batchelor type (Figure 25(c)). As we get closer to the axis, the centrifugal Ekman layer on the rotor disappears because of the centripetal flow. In this case it happens at $r* = 0.56$ (Figure 25(b)). The entrainment of the rotating fluid is then uniform from the rotor to the boundary layer of the stator with $V_\theta^* = 1$. Finally, close to the axis (Figure 25(a)), the imposed flow dominates the rotational effects and the two boundary layers are centripetal. At this radius, $r* = 0.44$, it is important to notice that in the cavity the swirl ratio can exceed the unit value ($V_\theta^* = 1.4$).
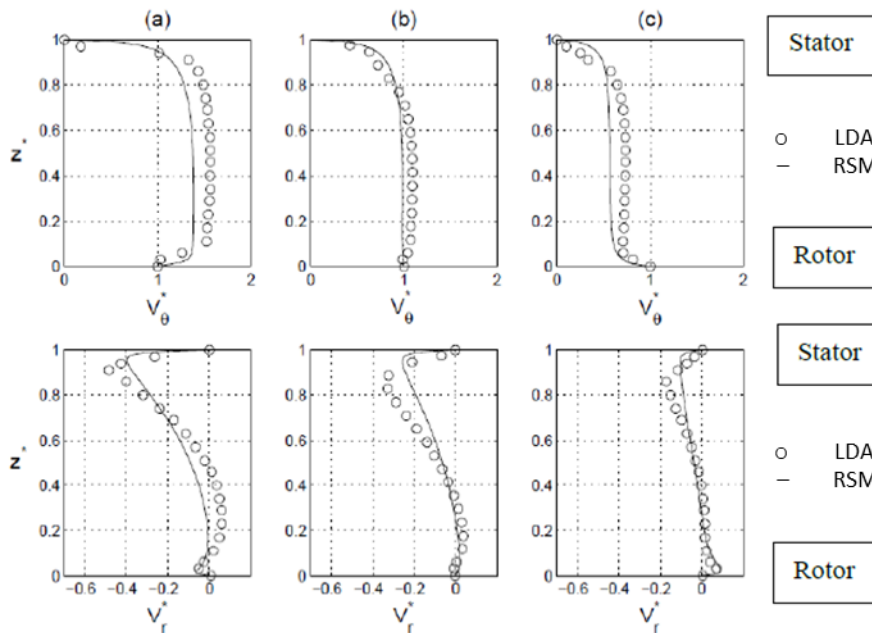
Figure 25 Radial and tangential velocity profiles in a cavity with centripetal flow, r=0.44-0.56-0.80*

Figure 26 shows the streamlines for this case:
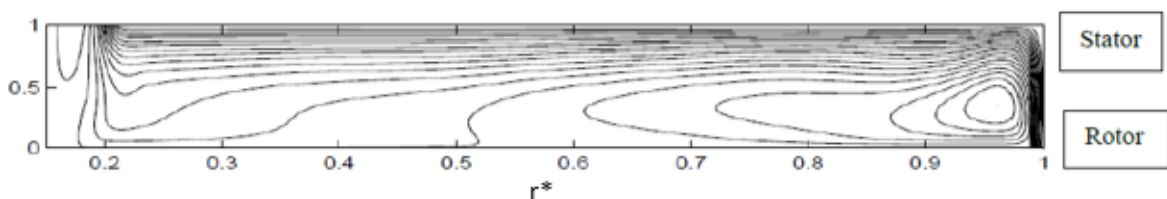
Figure 26 Streamlines in the cavity with centripetal flow

30

The imposed flux enters axially on the rotor side and impacts the stator before flowing towards the center of the cavity and exits axially on the stator side. Nevertheless, a re-introduction of the fluid into the cavity is observed at the level of the exit close to the axis.

In his work Poncet characterized the radial profile of the flow pressure. Figure 27 shows the isobaric lines for $G=0.036$, $Re_\theta=1,04.10^6$ and the three $C_w=-1976, -5929, -9881$. The isobars are parallel to the axis of rotation of the cavity. Apart from the recirculation zones, the pressure measured on the stator is the same as that measured on the rotor.
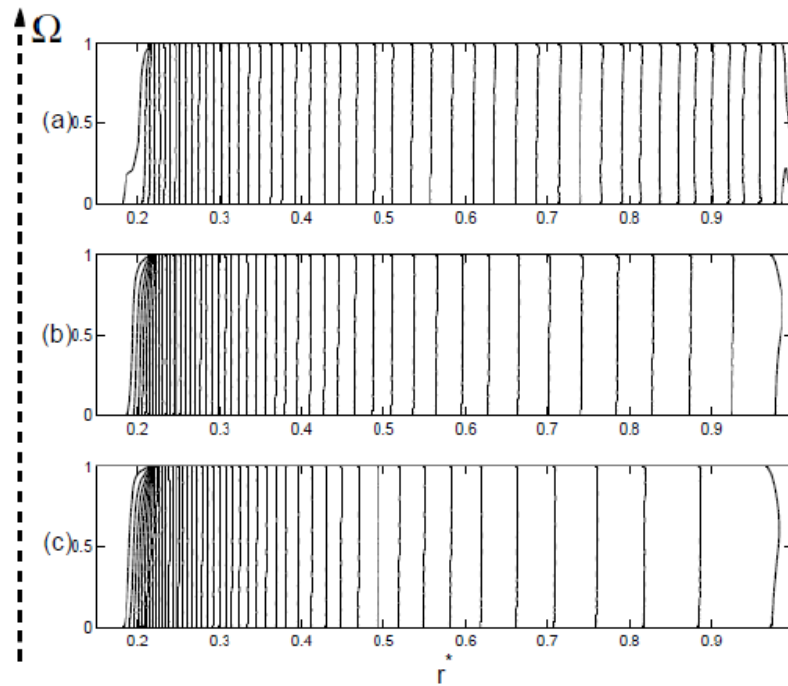
Figure 27 Isobaric lines of pressure for three increasing flows

S. Poncet makes a direct link between the increase in the coefficient K and the increase in the dimensionless pressure gradient:

$$p^* = \frac{2p}{\rho\omega^2 R_2^2} \tag{23}$$

He makes the justified assumption that in the core of the flow, only the pressure forces balance the centrifugal force:

$$\frac{dp^*}{dr^*} = 2K^2 r^* \tag{24}$$

This simple analytical equation makes it possible to relate the pressure gradient to a given radius as a function of training. The pressure gradient increases as $r*$ and as K^2. As the

31

imposed centripetal flow increases, K increases and so the radial pressure gradient between the axis and the cavity exterior intensifies.

Confined cavity with imposed centrifugal flow

Regarding a case with centrifugal flow ($Re_\theta=1,04.10^6$, $C_w=5929$ and $G=0.036$), the flux enters axially on the stator side and impacts the rotor before flowing out of the cavity then exits axially on the rotor side (shown in Figure 28).
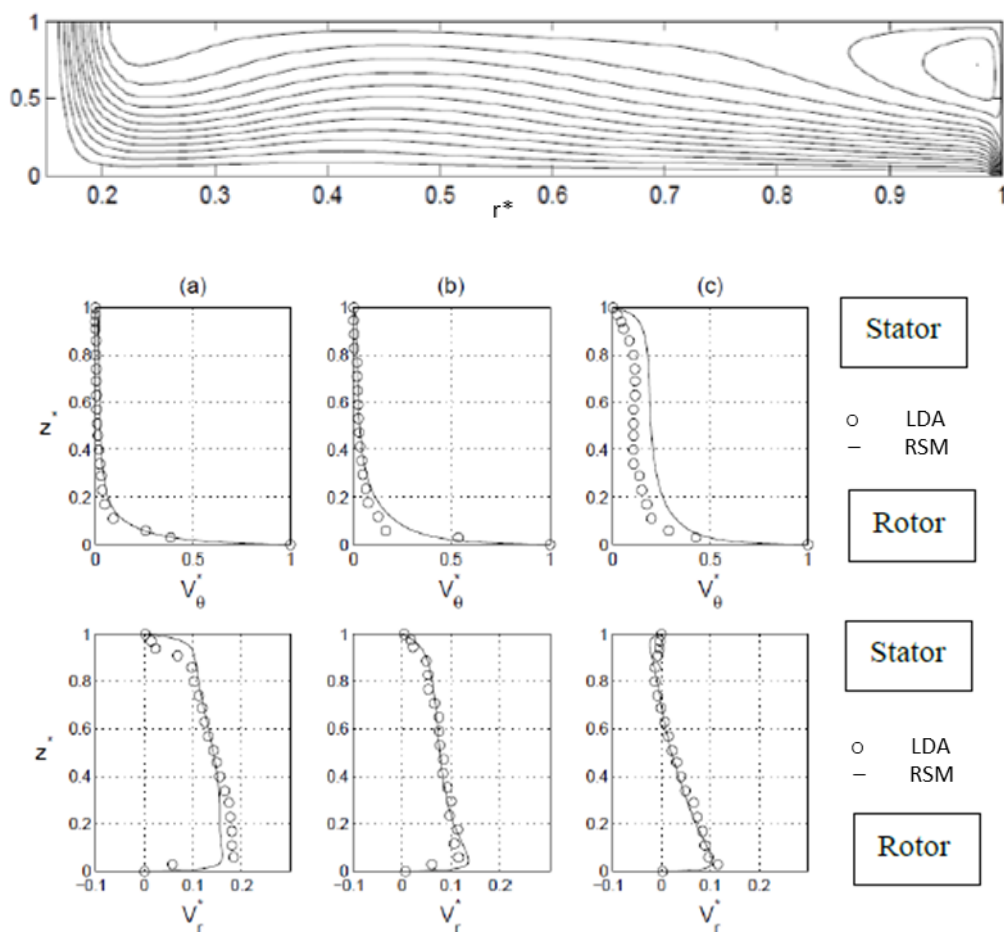
Figure 28 Streamlines, radial and tangential velocity profiles in a cavity with centrifugal flow, r*=0.44-0.56-0.80

Close to the axis of rotation, the flow is dominated by the impact of the axial jet on the rotor. On the contrary, far from the axis, rotational effects dominate and the velocity profile is characteristic of closed rotor-stator cavity flow (Batchelor).

32

If we observe in more detail, close to the axis (a), only the boundary layer of the rotor is in rotation: the flow is of the Stewartson type and is centrifugal from the rotor to the stator. Between $r*=0.56$ (b) and $r*=0.80$ (c) the radial flow direction in the Bödewadt layer starts to reverse into a centripetal flow, reaching a transition between Stewartson and Batchelor type. Furthermore, it can be noticed that the swirl ratio V_θ^* increases with distance from the axis and it reaches its maximum at $r*=0.8$, where $V_\theta^*=0,2$. We have to notice that this ratio is much weaker than in the case of the centripetal imposed flow.

By varying C_w, S. Poncet shows the dependence of the two types of flow (Batchelor or Stewartson) on the imposed Reynolds throughflow number.
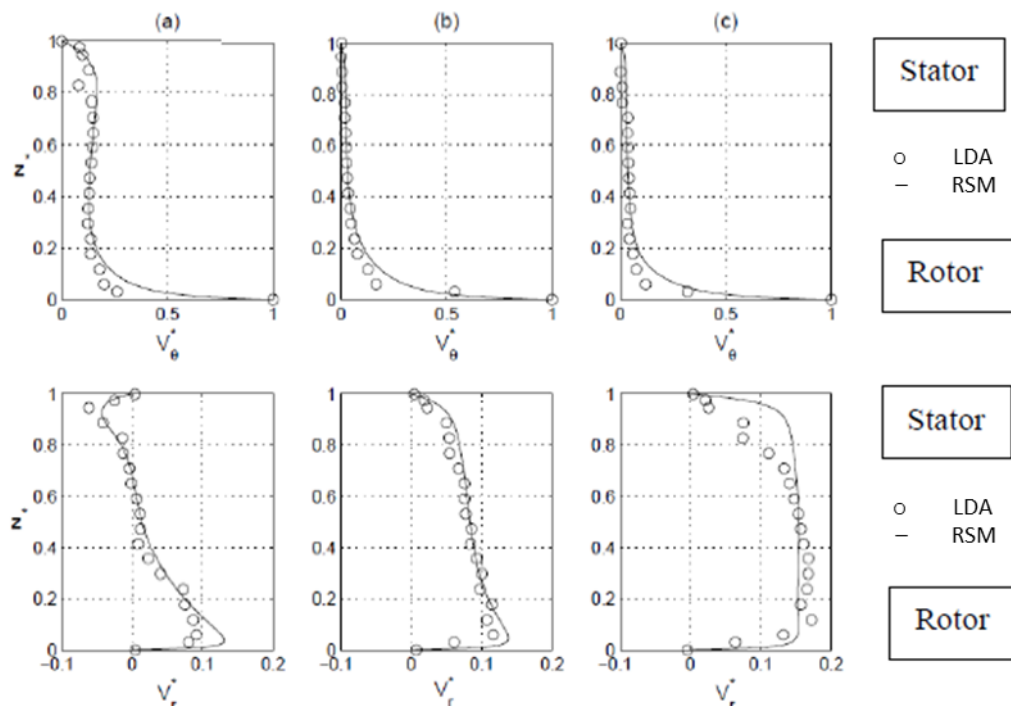
Figure 29 Velocity profiles for three increasing centrifugal flows at r*=0.56

When a low centrifugal flow ($C_w = 1976$, Figure 29(a)) is imposed, the flow keeps the same characteristics as in the case of a closed cavity: two boundary layers separated by a central core, which is known to be a Batchelor type flow.

By increasing the centrifugal flow, i.e. by increasing the flow coefficient ($C_w = 5929$, Figure 29(b)), the central core disappears and the flow becomes purely centrifugal. The axial profile of the tangential velocity is then of the Stewartson type. The axial profile of the radial velocity is greater near the rotor than near the stator. This indicates that a slight effect of the rotation remains.

For higher flow rate ($C_w = 9881$ Figure 29(c)), the axial profile of the radial velocity becomes symmetrical and approaches those encountered in a canal flow. An increase in the flow coefficient moves downward the transition from the Batchelor type flow to the Stewartson type. At position $r*=0.56$, the transition occurs for a flow coefficient between $C_w=1976$ and $C_w=5929$.

We can conclude the study of Poncet with the synthesis of the evolution of K as a function of C_w and $r*$ in the rotor-stator cavity with imposed centrifugal flow in the figure below:
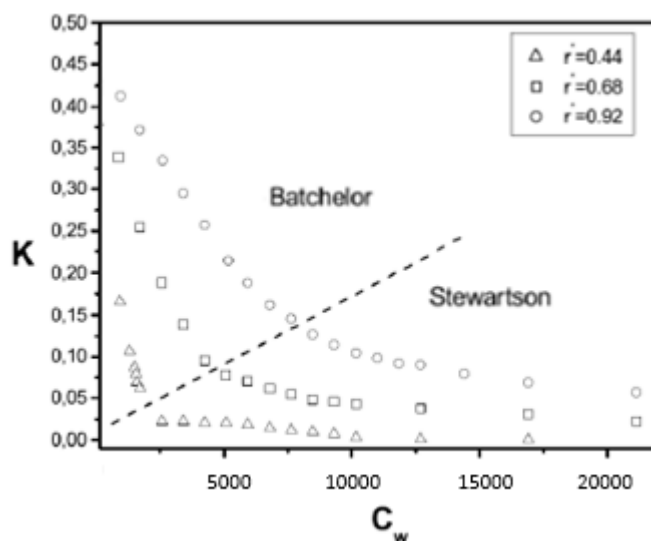
Figure 30 Swirl ratio as a function of the flow rate and the distance from the axis

K decreases with the increase in the centrifugal flow both when the flow is Stewartson type and Batchelor type. In particular, where the flow is Stewartson type, K decreases following an asymptote that depends on Re_θ and r*. Regarding the influence of r*, K is generally higher for higher r*.

4.1.2 Meshing and setup

As specified previously, the dimensionless quantities will be used for a greater simplicity of post-processing the results. In the following, $z*=0$ corresponds to the rotor surface while $z*=1$ corresponds to the stator surface. Figure 31 shows the geometry used for our simulations. It was taken by the internship report of *Schreck* [21], who started to study this rotor-stator system in SAE.
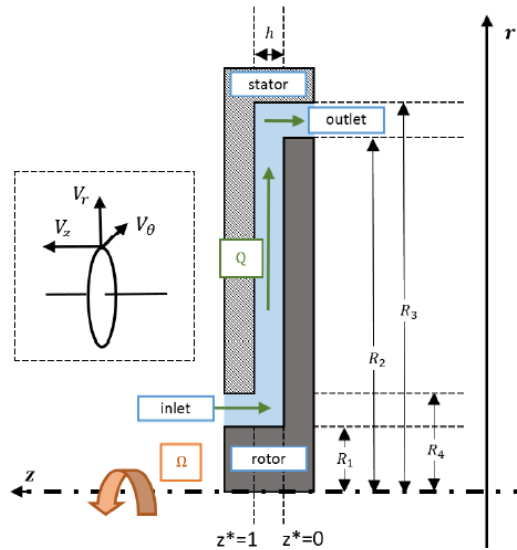
Figure 31 Poncet Test Rig, Geometry used in Fluent

In order to have a good mesh, some fundamental rules must be respected, such as:

- Ortogonal quality > 0.1
- Skewness < 0.9
- Between 10 and 20 prism layers.

From now on, all the meshes presented will respect these criteria with an orthogonal quality higher than 0.8 (on average) and a skewness lower than 0.2 (on average). As for the mesh influence, three different meshes have been designed to be able to coarsen as much as possible and analyze any differences in the results. In general, the mesh has spheres of influence in the conjunction between the entrance, the exit and the vertical wall, to avoid the possible propagation of errors in that area.
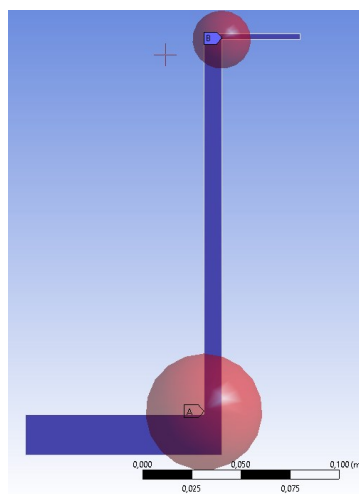
Figure 32 Sketch of the computational domain (blue) and sphere of influences (red)

35

Windage Correlations for Flows in Rotor-Stator Cavities

The two substantial differences for the three meshes are in the choice of the size of the first prism layer and the number of prisms. Based on this, the size of the elements is chosen, remaining however within the limit in which the cell must be inferior or equal to 10% of the smallest element of the geometry.

The three meshes are characterized as below:

- First mesh: 18 Prism layers, first prism layer 2.10^{-6} m
- Second mesh: 15 Prism layers, first prism layer 5.10^{-6} m
- Third mesh: 15 Prism layers, first prism layer 1.10^{-5} m

We can therefore notice a big difference between the first and the third mesh, which brings more than twice the size of the elements in general for the third mesh compared to the first. The difference as regards the number of elements is a ratio of 2.75 circa.

In the three meshes, however, it is of fundamental importance to have the $y^+ < 3$, i.e. the non-dimensional wall distance.

A non-dimensional wall distance for a wall-bounded flow can be defined in the following way:

$$y^+ = \frac{u_* y}{\nu} \tag{25}$$

Where u_* is the friction velocity at the nearest wall, y is the distance to the nearest wall and ν is the local kinematic viscosity of the fluid. y^+ is commonly used in boundary layer theory and in the definition of the law of the wall (see appendix 2 for more information).
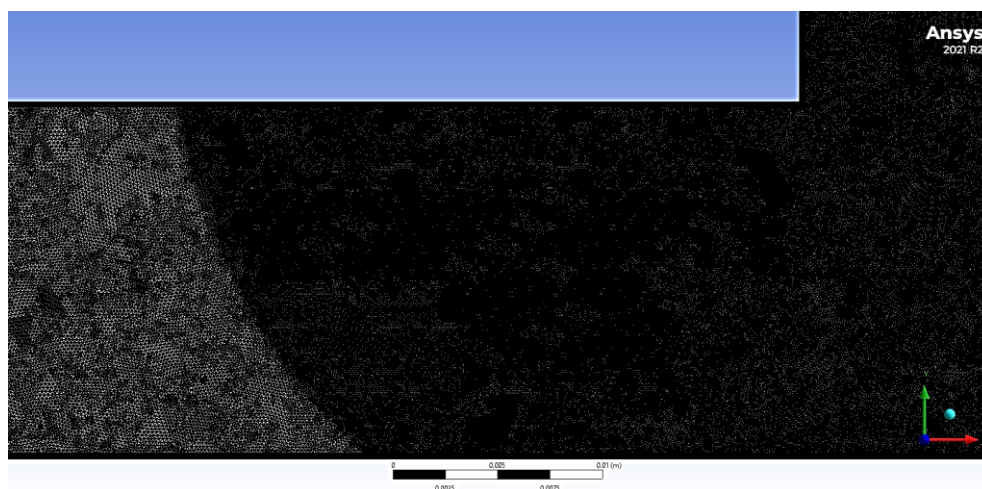
Figure 33 First Mesh

36

The first mesh is shown in the figure above, the third one in the figure 34 below, to see the differences. The two figures show a detailed view of the cavity entrance and the first sphere of influence.
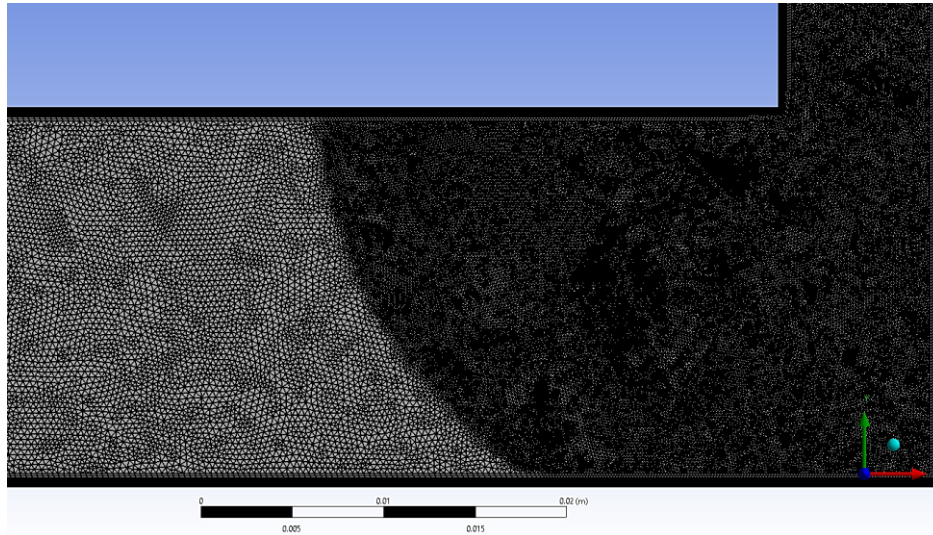
Figure 34 Third Mesh

Regarding the Fluent setup, the following choices were made (later used throughout the thesis):

- Type: Pressure-Based
- Velocity Formulation: Absolute
- Time: Steady
- 2D Space: Axisymmetric Swirl

The boundary conditions were:

- Inlet: Mass flow inlet
- Outlet: pressure outlet
- Rotor: Moving wall
- Stator: Stationary wall

More information about the strategy of convergence will be given in chapter 6.

For the post-processing of our results, different radii r^* are studied, i.e. r^*=0.44-0.56-0.80 as shown in the figure below. We place ourselves at r^*, and at this fixed radius we see the variation of the radial and tangential velocity as a function of the z^* coordinates.

Windage Correlations for Flows in Rotor-Stator Cavities
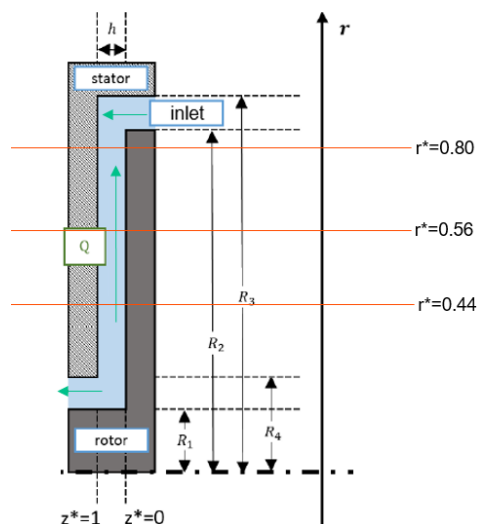
Figure 35 Radii for the post-processing in Fluent

Once the three meshes were created, some simulations were launched to be able to see the difference, if any, between the three cases. The following example shows the first of the three centrifugal cases, that is the case with the throughflow Reynolds number $C_w = 1976$ and $Re_\theta = 1,04.10^6$. In this case, the radius for the post-processing is $r^*=0.56$.
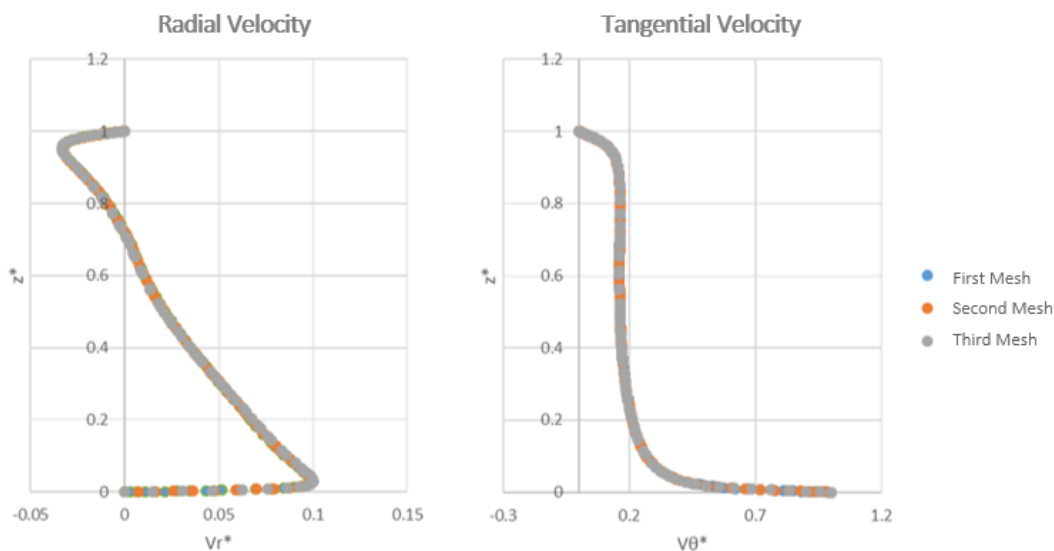
Figure 36 Fluent velocity profiles for the three meshes, Poncet's Case1, r=0.56*

As seen in 4.1.1, this is a Batchelor-type flow with the Ekman layer, the Bödewadt layer and the solid rotation. Through the figure above, we can well observe that there are no differences between the three meshes as regards the radial and tangential velocity profiles, the three curves are perfectly superimposed. However, in order to compare these three calculations

well, although there are no comparable experimental results, the convergence of the moment on the rotor and stator surfaces has been analyzed.

The results are in the following table:

	Moment Rotor [Nm]	ε%	Moment Stator [Nm]	ε%
First Mesh	0.1327		0.0426	
Second Mesh	0.1326	-0.075	0.04275	+0.352
Third Mesh	0.1328	+0.075	0.04272	+0.281

Table 2 Differences in moment for the three meshes

Therefore, taking as a reference the first mesh, much finer and therefore with a higher precision level, we see how the error between the various meshes is completely negligible, which therefore tells us that the convergence in mesh is correct.

4.1.3 Influence of Turbulence models and first results

A study on turbulence models was done in order to choose the best one for our needs. The study was carried out between:

- k-ε realizable
- k-ω SST

To have more information about the turbulence models see appendix 3. In order to see the differences between the two turbulence models, we can start the comparisons between our results and the Poncet's work. As we said, Poncet studied his test rig experimentally (LDA) and also with RSM approach (Reynolds Stress Model).

In this work, we will compare both approaches to observe first if the results are consistent with the experimental measurements and then if they are close to RSM modelling (in Poncet's opinion RSM is more accurate than the two models used in this work). The results shown are for the second and the third centrifugal case studied:

Windage Correlations for Flows in Rotor-Stator Cavities
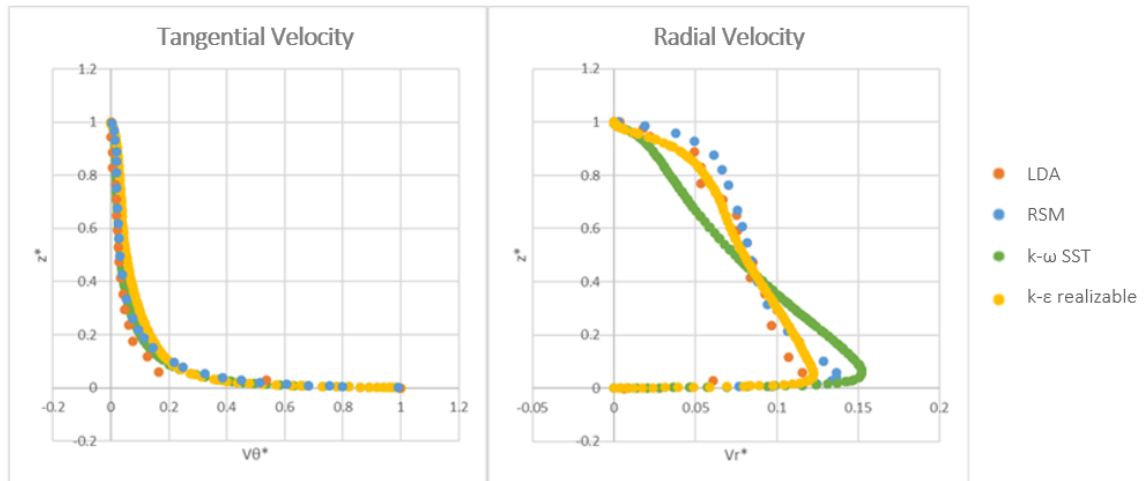
Figure 37 Velocity profiles for Poncet's Case2, r*=0.56

The Figure 37 above shows the results for the case C_w=5929 and the Figure 38 the velocity profiles for the case C_w=9881. The flow is of the Stewartson type and is centrifugal from the rotor to the stator. As we can see in these figures, the realizable k-ε turbulence model gives much more consistent results than the k-ω SST model. In fact, regarding the radial velocity profile, k-ω SST model doesn't predict the same flow as the LDA measurements (red circles). We can observe that, both in the Ekman and in the Bödewadt layer the radial velocity profile is not the same at all.
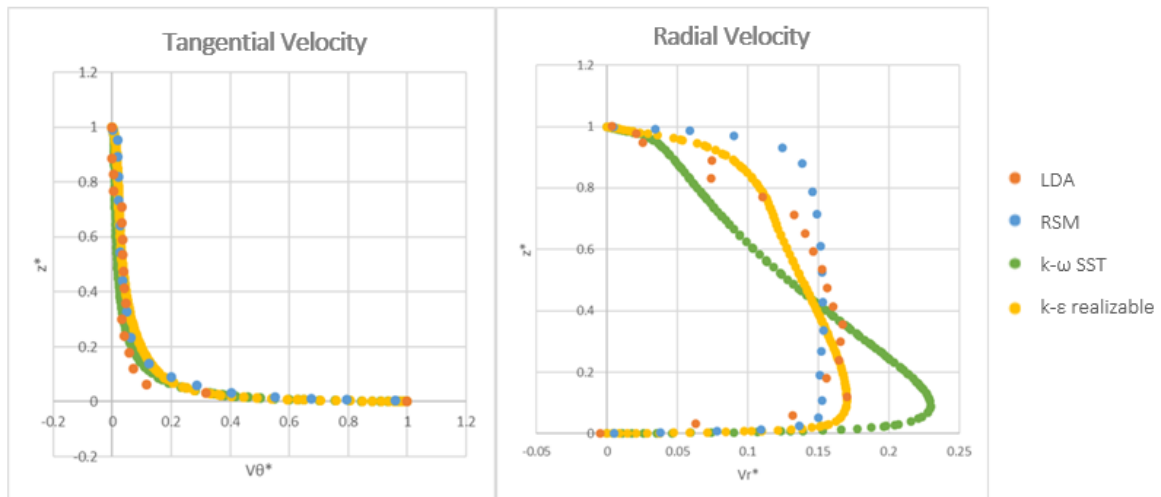
Figure 38 Velocity profiles for Poncet's Case3, r*=0.56

Otherwise, regarding the tangential velocity, there is not much difference, both follow the experimental results quite well. In general, we also see how the results of k-ε turbulence model are very consistent with the LDA experimental results. As regards the RSM approach,

40

a difference is visible above all in the case3 ($C_w = 9881$) in which our Fluent model is able to pick up the area near the wall $z^* = 1$ well, that is the stator wall, better than the blue curve (Poncet's RSM).

To finish the first academic test cases we show some results of the extreme case and the centripetal case.

4.1.4 Application to centrifugal and centripetal flows

As for the extreme case, we recall that it has been defined as "extreme" because it uses the highest data values of C_w and Re_θ from the Poncet's thesis, that is $C_w = 10317$ and $Re_\theta = 4,15.10^6$. This case also served to analyze the robustness of Fluent and the y^+ of the surfaces, which never exceeded the value 3. The display mode of the results is the same as the previous ones, we position ourselves at $r^* = 0.56$ and see the variation of the velocity profiles. Figure 39 shows the extreme centrifugal case, it is a Batchelor-type flow. It can be noticed how the Fluent model is able to capture the radial and tangential velocity profiles very well, the curves are practically superimposed with the LDA results, and, in some points, more accurate than the RSM model. The percentage error in K is about 2%.
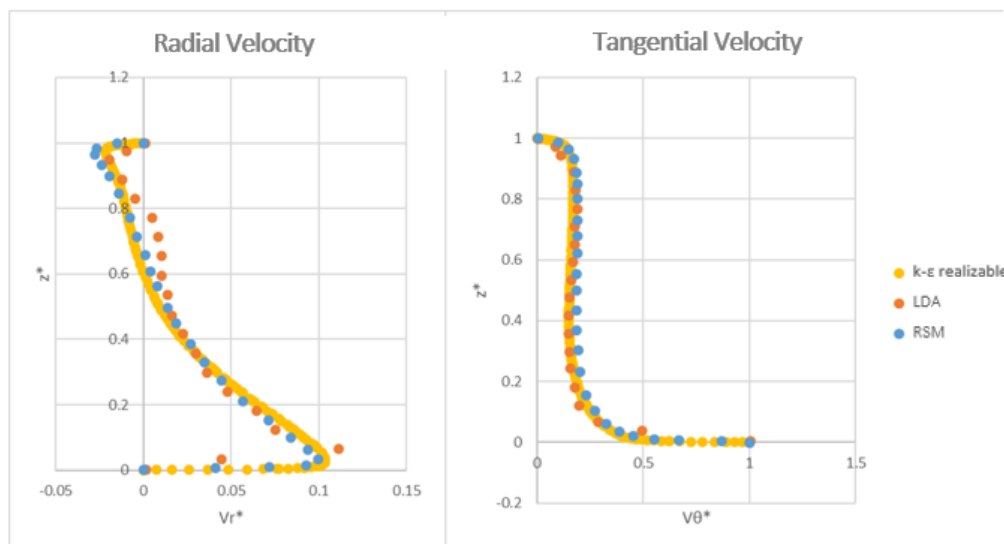
Figure 39 Velocity profiles for Poncet's Case4, r*=0.56

Only a small part is not able to be captured with our model (and that not even Poncet did), near the stator zone.

Windage Correlations for Flows in Rotor-Stator Cavities

As for the centripetal case, some problems were found on the convergence of the simulation, which was less stable. In fact, in the centripetal case, the flow is substantially the opposite, the entrance becomes the exit and vice versa. The flows enters an area that has a very small diameter, consequently there is a slight initial instability which takes some time to recover. In general, to solve this problem, a longer inlet length has been adopted, so as to make the flow stable, which, being in a very narrow area (3 mm), approaches a $K = 0.5$ (much influence of the angular velocity of the rotor).
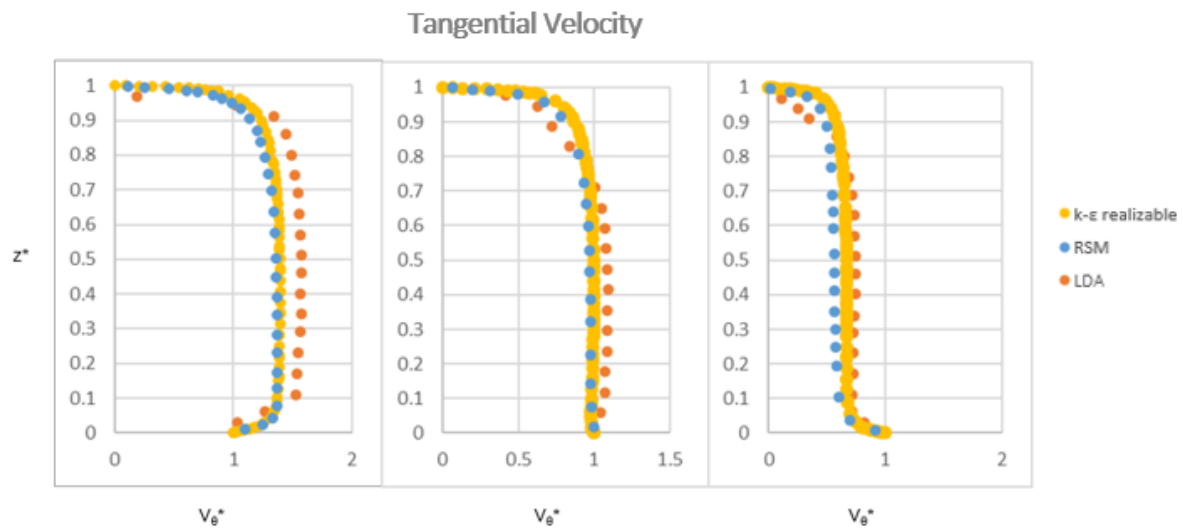
Figure 40 Tangential velocity profiles for Poncet's Case6, r*=0.44-0.56-0.80

Figure 40 shows the results of the tangential velocity in comparison with Poncet. We can see that the curves are quite consistent with the LDA curves but not as much as the centrifugal cases. The percentage error in K is up to 11% (r*=0.44). Furthermore, it can be noted that in some cases, especially at large radii, the Fluent simulation is slightly better than the RSM approach.

Stopping therefore at these simulations, we could see how, in general, the k-ε realizable model is much more consistent than the k-ω SST model. The results are satisfactory as regards the speed profiles.

In the next section we will also focus on the moment coefficients thanks to other experimental results. Experimental data on the moment coefficients are fundamental for validation of our work since it is precisely from the moment generated on the surfaces that the windage losses occur.

4.2 Bolt Windage Rig

The Bolt windage test rig shown in Figure 41 is a general assembly of the test rig used for experimental measurements at the Thermo Fluid Mechanics Research Centre (TFMRC) at Sussex University by *Coren* [4] and *Miles* [13]. This consists of a shaft-mounted titanium alloy disk with an outer radius of $b = 225$mm enclosed within a sealed steel pressure casing.
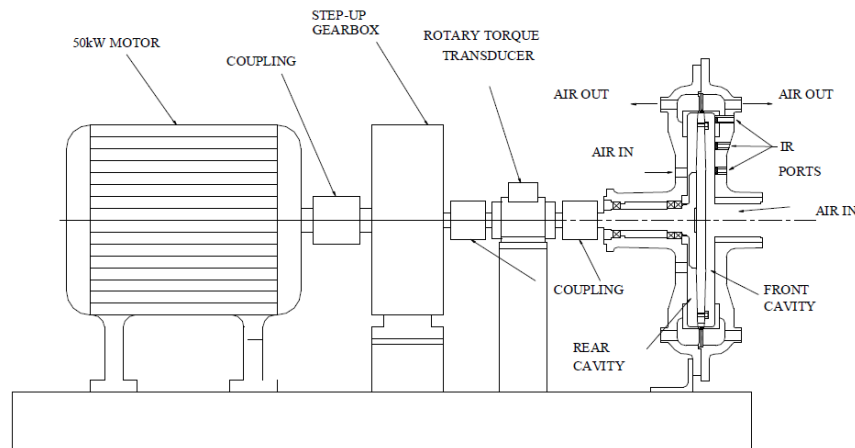
Figure 41 Bolt windage Rig, University of Sussex

The maximum clearance between the rotor and the casing is $s = 22$mm, but the gap is not constant. At the end of the cavity (rotor) there is a labyrinth seal and a stator-mounted shroud encases the cavities on either side of the disk. The test side of the disk is the front cavity, the rear cavity balance the flow conditions on both sides of the disk. A superimposed flow of air enters the rig axially and flows radially outward through the cavity.

The labyrinth seal at the end of the cavity regulates the flow out the rig. An equal amount of air is supplied to the balance side, where it enters through four inlet pipes equally spaced around the central shaft. There are four orifice plates positioned downstream and upstream of the test rig on both the test and balance side to measure the mass flow of air into and out of the rig. The simulations covered the following range of dimensionless parameters that are typical for a gas turbine engine:

$$0,27.10^7 \le Re_\theta \le 1,4.10^7$$

$$0,3.10^5 \le C_w \le 1.10^5$$

$$0,06 \le \lambda_T \le 0,58$$

Windage Correlations for Flows in Rotor-Stator Cavities

The torque due to bearing friction in the test rig depends on rotational speed and was subtracted from all of the measured values of torque to obtain a value of the torque transmitted to the fluid.
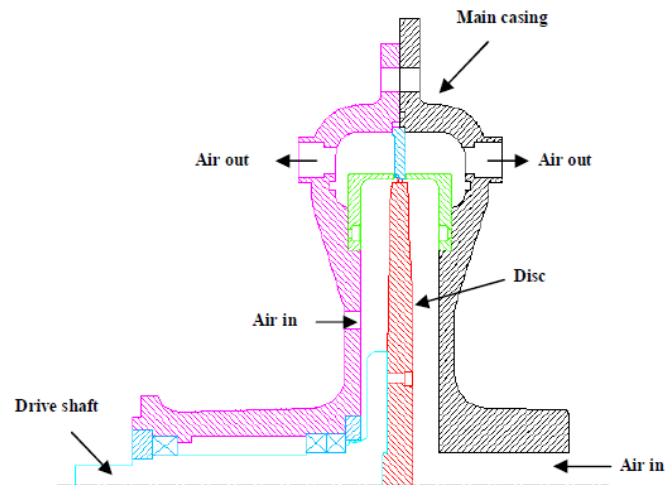
Figure 42 Bolt windage Rig, configuration studied

Coren and *Miles* worked on this test rig. The aim of Coren's work was to establish correlations between the magnitude of windage as a function of the size, location and orientation of protrusions over a range of real engine conditions. The test rig has been built to perform experiments which allows a direct torque measurement. Velocity profiles have also been studied with the aid of Laser Doppler Anemometry (LDA) to observe the flow velocities and directions around the protrusions. Before testing the protrusions, Coren developed a first test with a plain disc, i.e. without protrusions. The results of this work would also provide data which could readily be compared to existing correlations and theoretical results for plain discs. Furthermore, Coren investigated the effect of spacing and radial location of 16 mm hexagonal bolts on windage. From his work, he understood that when two rows of bolts are present, rotor bolts at a high radius contribute more than low radius bolts to total windage. Moreover, stator bolts tests showed that two rows of bolts produces lower values of windage than the plain disc, whereas a single row at high radius gave either similar or higher than plain disc values. It was also shown that the number of rotor bolts, and consequently the circumferential spacing, has a significant effect on the measured windage.

Miles continued the works of Coren to determine the effect of protrusions on windage and rotor surface temperature. She varied the diameter of hexagonal rotor blots (protrusions

found in a variety of gas turbine applications) but also tested bi-hexagonal bolts (especially used in aeronautics applications). Also Miles, started her test cases by the plain disc, in order to compare her results with the results of Coren's works.

Figure 43 shows the moment coefficient C_m, his variation with the rotational Reynolds number Re_θ, for the plain disk results from Coren's works. The more physically realistic solutions of *Dorfman*, and *Bayley* and *Owen*, were selected for comparison by *Coren*. We can see observable differences between the data but these differences may be understood by plotting the Sussex data only where $\lambda_T \approx 0,2$ (Figure 44).
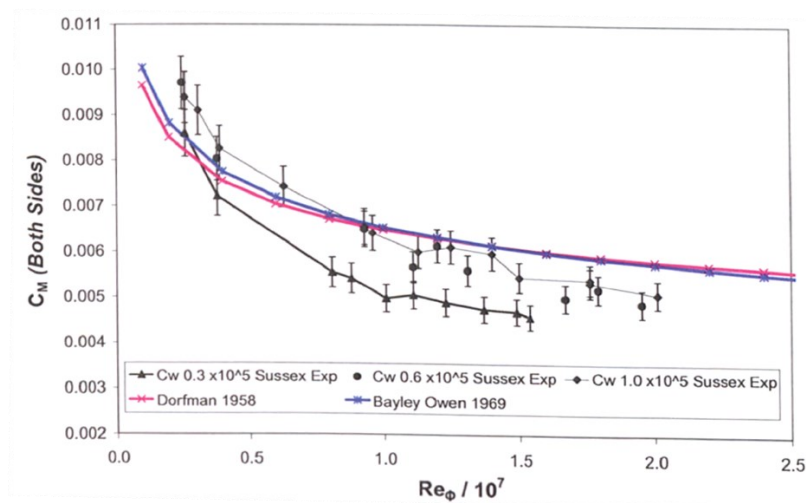
Figure 43 Cm as a function of Reynolds number with correlations, Coren

If we plot the data only for $\lambda_T \approx 0.2$, we observe a good agreement between the data. This is because when $\lambda_T \approx 0.2$, the maximum entrainment rate for the disk system is reached, and the fluid regime in the rig is similar to that of a free disk.
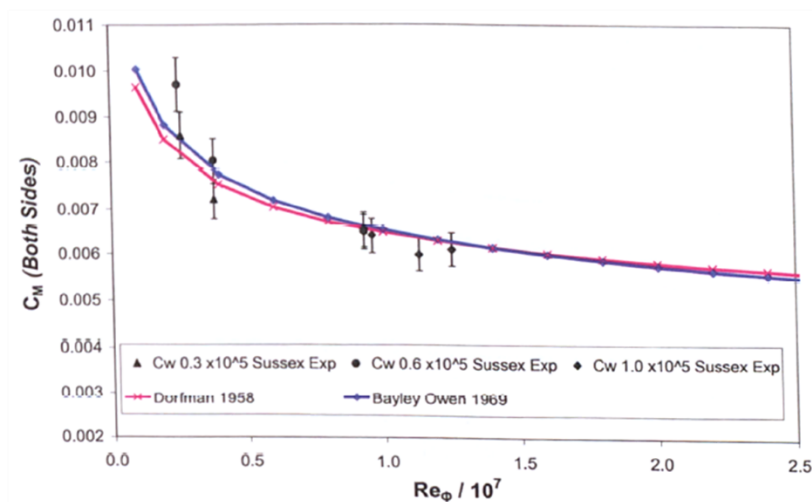
Figure 44 Cm as a function of Reynolds number for $\lambda_T \approx 0.2$, Coren

45

Figure 45 below shows the comparisons between Coren's and Miles'results. In this figure, we can observe that, when the rotational Reynolds number is low, the uncertainty is really high, while, in the case of a high Re_θ it becomes really small.
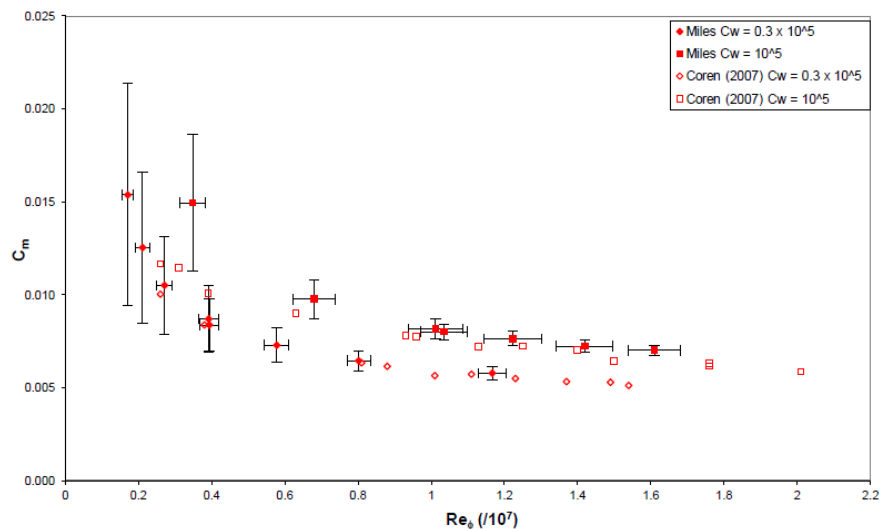
Figure 45 Cm as a function of Reynolds number, Coren and Miles

There is generally good agreement between the two sets of data. Miles observed that Coren measurements were within 4% of her results in the case of $C_w = 0,3.10^5$ and within 8% in the case of $C_w = 10^5$, except for the case with a lot of uncertainty ($Re_\theta = 0,35.10^7$).

Miles compares her work also with the correlations for a rotor-stator system with throughflow from Owen [9] and Gartner [12]. For $\lambda_T < 0.219$ she found a good prediction of the windage test rig, with an increase if $Re_\theta > 1,2.10^7$.
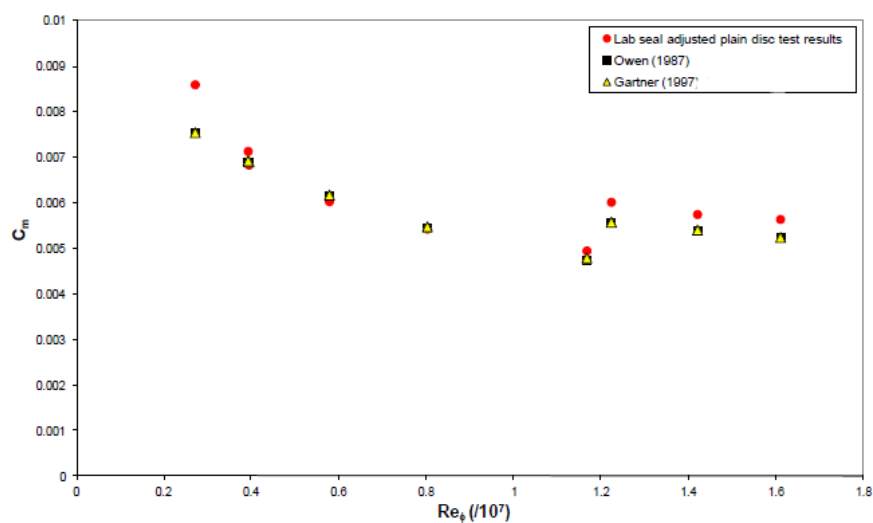
Figure 46 Comparison between Miles's results and rotor-stator correlations, $\lambda_T < 0.219$

For $\lambda_T > 0.219$, Owens model give better agreement than Gartner's model.
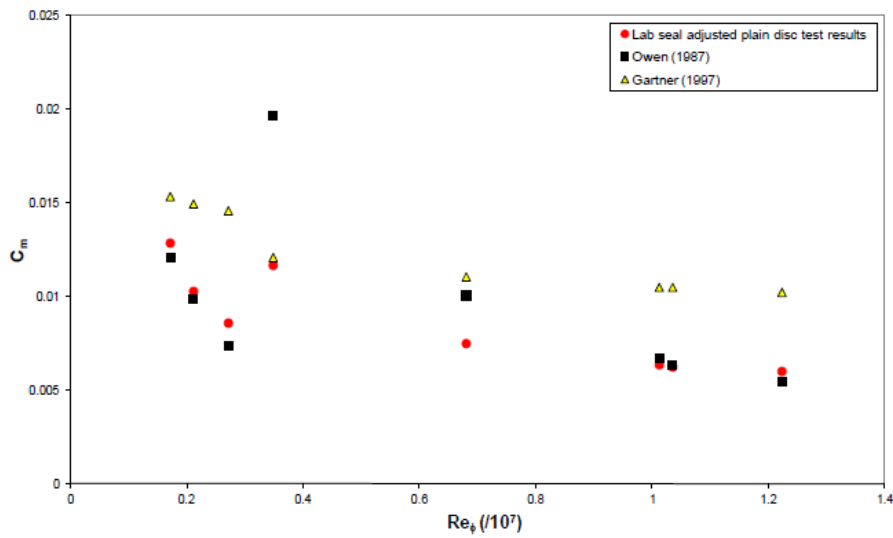
Figure 47 Comparison between Miles's results and rotor-stator correlations, $\lambda_T > 0.219$

Lastly, the figure below shows also the variation of the moment coefficient with Reynolds number and the correlations of *Daily et al.* for $0.063 \leq \lambda_T \leq 0.601$. Predictions of *Daily et al.* is very good, except where $Re_\theta < 0,4.10^7$, a region in which the experimental uncertainties become relatively large.
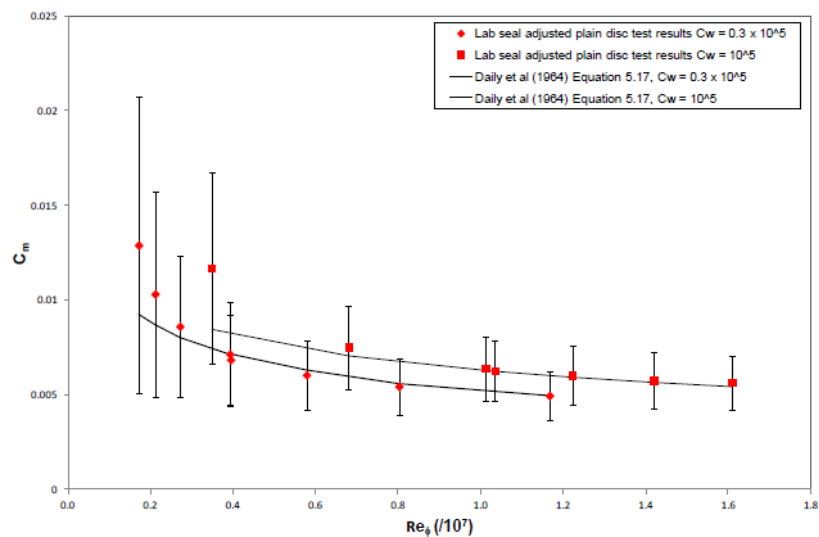
Figure 48 Comparison Miles's results with Daily et al

4.2.1 Simulation of the Bolt windage Rig

Coren's results were used to compare the moments on the rotor surface and some velocity profiles. Miles' results were used to compare moments on other cases and finally Moghaddam's work to qualitatively compare the Fluent model and the velocity profiles found.

For the three theses the geometry used is the following [14]:
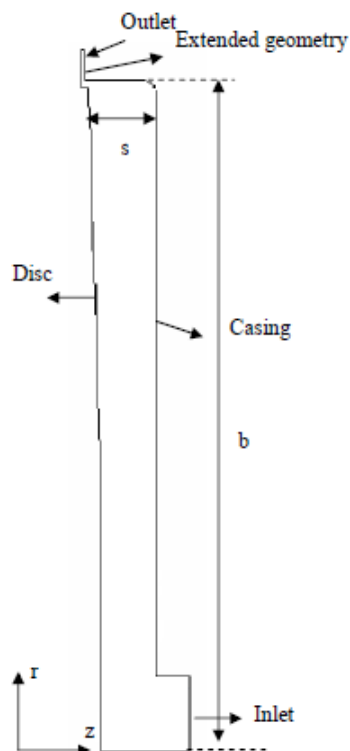
Figure 49 University of Sussex – Test rig' geometry

There is an extended geometry after the outlet, which is used to avoid reversed flow through the outflow boundary. This extended geometry provides a uniform flow before the outlet boundary and prevents it from changing direction and re-entering through the outlet, which could cause numerical instability.

Full geometric data was not available. Some assumptions were made, in particular on the location of the max disk/stator clearance, leading to an uncertainty of 1mm.

Furthermore, as we said in the description of the test rig, at the outlet there is a labyrinth seal, to control the exit of the flow through the cavity. This zone causes losses which must be subtracted from the total moment.
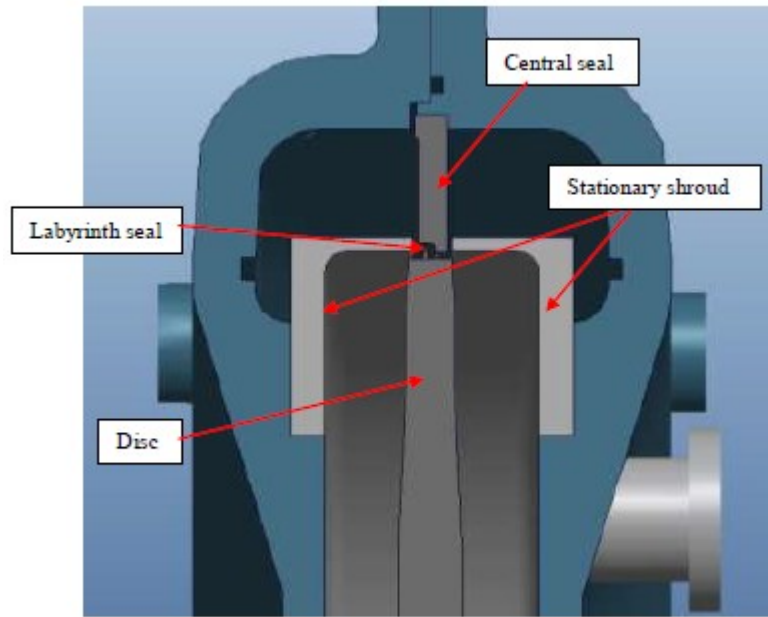
Figure 50 Labyrinth seal, Bolt Windage Rig (Moghaddam)

The moment generated by the labyrinth seal is defined by the following formula from *Millward* and *Edwards* [22]:

$$M_L = C_{m,seal}\pi L\rho\omega^2 b^4 \tag{26}$$

The parameter $C_{m,seal}$ is the seal moment coefficient:

$$C_{m,seal} = 0.06\left(\frac{C_w}{Re_\theta}\right)^{0.55} n_f^{-0.65} \tag{27}$$

Where n_f is the number of fins (in this test rig $n_f = 2$) and L the length of the seal. Coren and Miles use a different length L for their works and therefore different losses for the moment coefficient. Moghaddam calculates these losses with Fluent by including the geometry of the seal in some of his simulation. The losses are the following:

- Coren: L=0.016 m, i.e. 14%-20% of losses of total moment coefficient
- Miles: L=0.0212 m, i.e. 16%-23% of losses of total moment coefficient
- Moghaddam: 11% of losses of total moment coefficient.

For our work, we will compare Coren's results with Coren's losses and Miles' results with Miles's losses, in order to be consistent with their works.

Also for the Bolt windage Rig, a mesh study was done but it was realized that, due to the already high Re_θ and C_w, it would have reached a $y^+ > 3$ in some cases studied. Consequently, the same parameters as the finest mesh for the Poncet's test cases have been retained. The calculations were made with both the k-ε realizable and k-ω SST turbulence models. Regarding the setup, it is the same as that used for Poncet's cases, with the only difference in Inlet (pressure inlet) and Outlet (mass flow outlet), based on available data.

4.2.2 Coren Test Cases

The case studies of Coren are the following two:

	Omega (rad/s)	Q (kg/s)	Re_ϑ / 10^7	C_w / 10^5	λ_T
Case1	408,41	0,122	0,26	0,29	0,21
Case2	921,53	0,128	0,81	0,3	0,09

Table 3 Two Coren's Cases

For the results, let's take Figure 43 of 4.2, thus adding the moments found through the Fluent calculations with the two turbulence models. In general, we can immediately point out that for both models of turbulence, the moments found are well within the uncertainties of the experimental works and that they are also consistent with them.
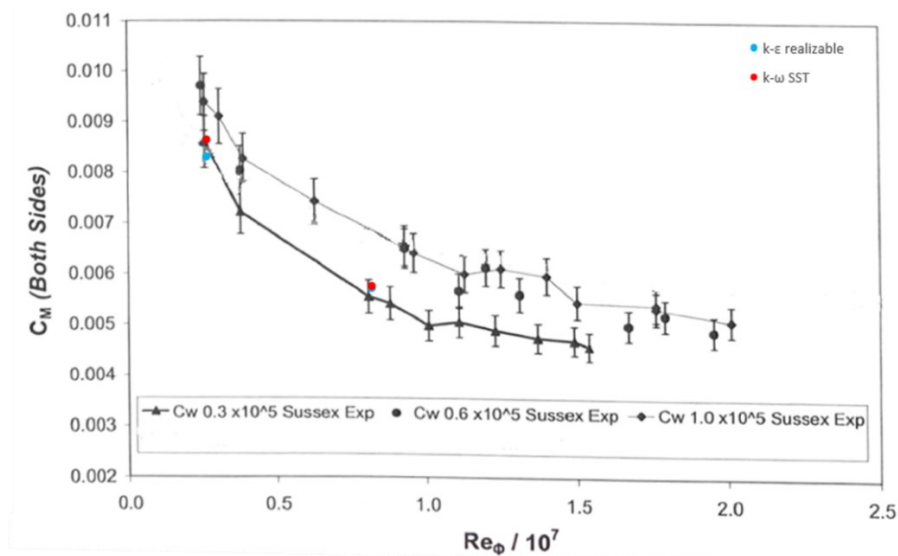
Figure 51 Moment coefficient – Coren's Cases

Furthermore, we can see how the two models, with a high Rotational Reynolds number, give almost the same results (overlapping blue and red circles).

We can translate this image into figures, taking relative errors on moments (N.m), and consequently on windage losses. The errors for the two cases are in the following table:

Case1	k-ε realizable	k-ω SST
Fluent	0,4689	0,4889
Coren	0,4839	
Erreur %	-3,08 %	1,04 %

Table 4 E% Case1 Coren and Fluent

Case2	k-ε realizable	k-ω SST
Fluent	2,3346	2,3507
Coren	2,2555	
Erreur %	3,50 %	4,22 %

Table 5 E% Caes2 Coren and Fluent

The errors for the two cases, and for both the turbulence models, are below 5%, which means accuracy is very good. We also observe that the k-ω SST model always tends to overestimate the result compared to the realizable k-ε model.

As seen previously, the moment coefficient depends on the coefficient C_f, which depends on the tangential component τ_θ. The two figures below show the radial profile in the cavity of the C_f in the axial position $z* = 0,5$ (see section 4.3 for more details).
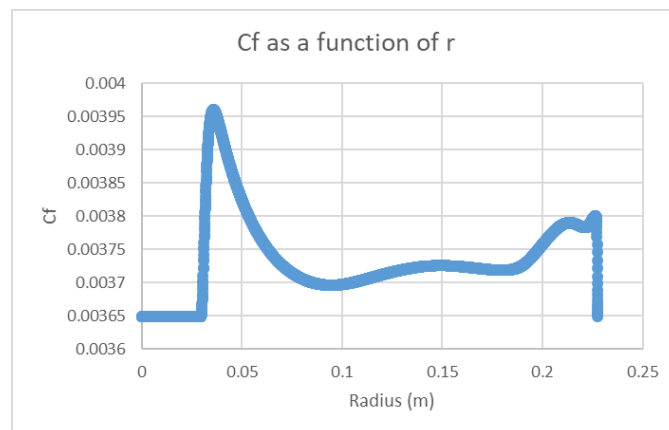
Figure 52 Cf as a function of radius, Coren Case1

51
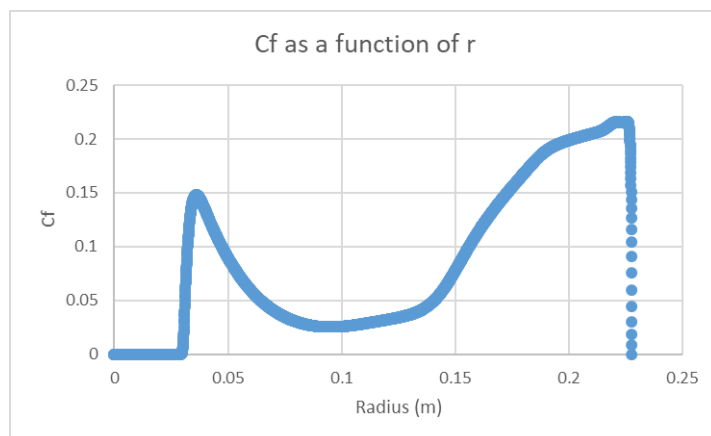
Figure 53 Cf as a function of radius, Coren Case2

In the first case, it is higher near the axis (low radius) and then increases slightly at high radius (this is where there are the greatest losses in a rotor- stator cavity).

If we look at the second case instead, we see how at high radius it is much higher than at low radius. This is explained by the type of flow. First of all, in the second case, the C_w is much higher, the flow arrives and impacts the wall in a different way, the recirculation bubble and the flow are different. In the first case, the flow is dominated by rotation, in the second one it is dominated by centrifugal flow, K tends to 0 and the friction between rotor and fluid is maximised.

Figure 54 Streamlines Coren's Case1 (left) and Case2 (right)

52

Regarding the velocity profiles, Figure 55 shows the Case1 of Coren.
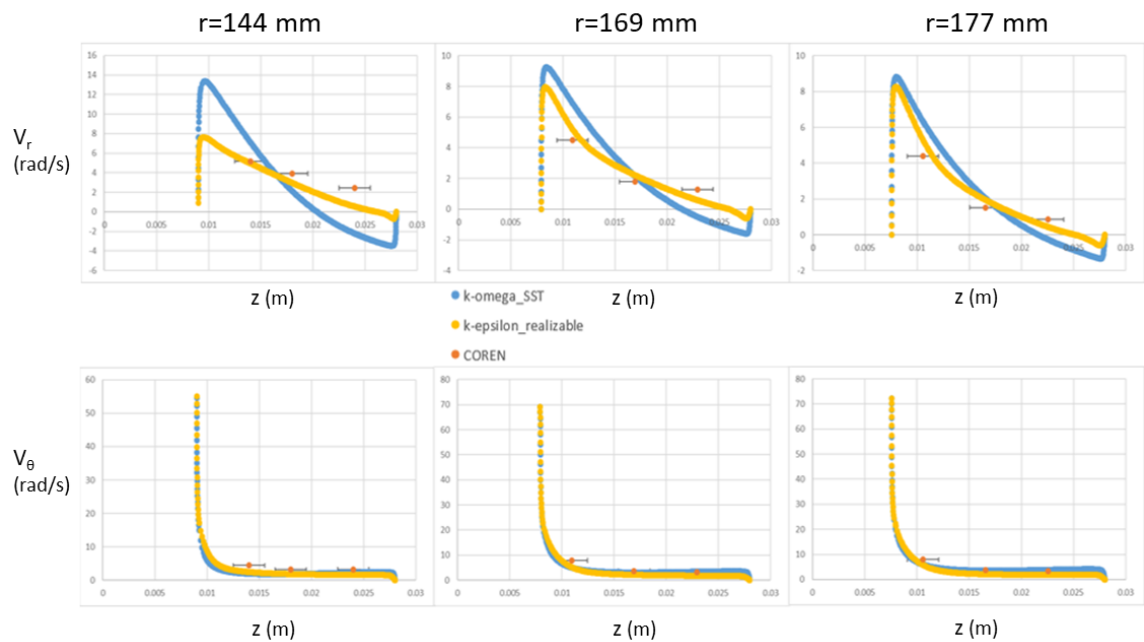
Figure 55 Radial and tangential velocity profiles, Coren Case1

In this case, the dimensional values are analyzed (the radius r and velocities V_r and V_θ). Coren, as Poncet, used the LDA measurement to find the profiles. For his work, the measurement volume length was of 3mm [4] that give the uncertainty in the Figure 55. Observing the figure, as noticed in 4.1.3, there is a small difference in radial velocity between the k-ε realizable model and the k-ω SST model, at a big radius. The difference increases when the radius decreases. For the tangential velocity profile, there is not much difference.

Moreover, in comparison with Coren's experimental results, we notice a better agreement for the k-ε realizable model.

The substantial difference between the two models can be explained based on the difference they have in quantifying the recirculation at the entrance to the cavity. Figure 56 shows the recirculation bubble in the cavity according to the two turbulence models.

The k-ω SST model (Figure 56 right) has a larger recirculation bubble than the k-ε realizable one (Figure 56 left). This therefore entails a substantial difference in speeds, which is especially visible in the case of the radial velocity profile.
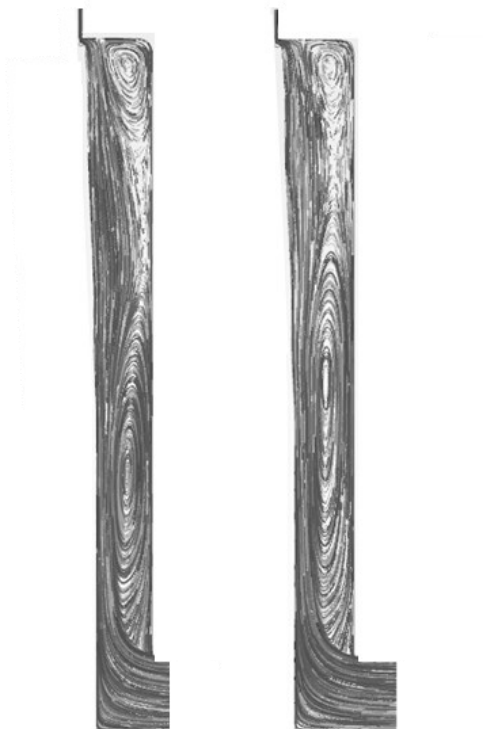
Figure 56 Streamlines Case1 Coren. k-ε realizable (left) and k-ω SST (right)

Although, there is not a lot of difference regarding the moment coefficient. In fact, as we said in the second chapter, the moment coefficient C_m depends on the tangential wall shear stress distribution and we noticed that, in our cases, the two turbulence models are quite similar for the tangential velocity component.

Therefore, considering the results obtained on Poncet's test cases and the latter ones, the k-ε realizable model appears to be most suitable choice. However, we still have one last comparison to do, with the four cases of Miles.

4.2.3 Miles Test Cases

Miles in her work uses the same geometry as Coren, with the difference in taking into account the losses generated by the labyrinth seal (see 4.2.1). We will therefore use the same methodology as in paragraph 4.2.2, taking up in this case Figure 45 for the comparison, which will be carried out with the k-ε realizable model (these tests cases were also modelled by Moghaddam). Miles' cases are the following:

	Omega (rad/s)	Q (kg/s)	Re_ϑ / 10^7	C_w / 10^5	λ_T
Case1	261,9	0,125	0,171	0,31	0,32
Case2	1057,4	0,123	1,167	0,286	0,063
Case3	207,5	0,413	0,348	1,029	0,6
Case4	1060,6	0,418	1,61	0,986	0,17

Table 6 Four Miles' Cases

For the results concerning velocity profiles, the Moghaddam CFD results were used. However, it must be said that the comparison was made qualitatively.

Moghaddam tried to model test cases from Coren and Miles using a Fluent 2D and 3D model (with and without bolts). We must therefore be aware that the two models are different. Moghaddam actually chose the standard k-ε model (in his opinion the best compromise for precision of results, calculation time and computational cost). Furthermore, the mesh was also different, with fewer elements than our mesh.

The following figure shows the results regarding the moment coefficients on the Reynolds number.
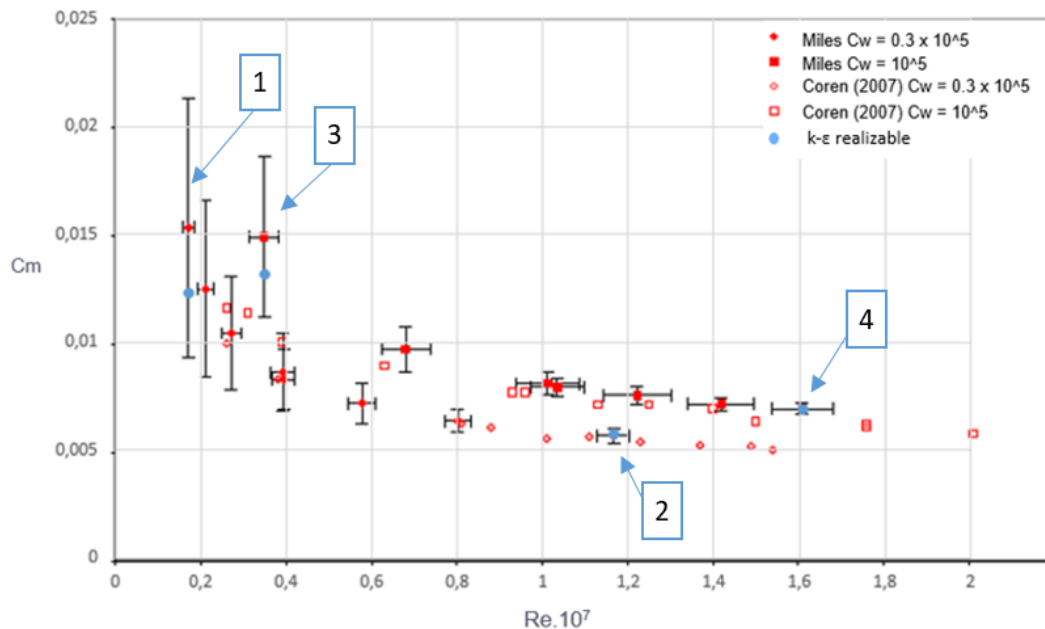
Figure 57 Moment coefficient – Miles' Cases

The k-ε realizable model is shown in blue. It was decided to verify some cases with a low Reynolds (Case1 and Case3) and some with a high Reynolds number (Case2 and Case4) in order to cover the range of cases.

Miles shows how in some test conditions the uncertainties are high, especially for the low Reynolds cases, so it is necessary to take it into consideration for our comparisons.

Looking, therefore, at the first two cases, we see how the moment coefficient is well within the uncertainties of Miles' experimental results, but not entirely consistent with the value found by the experiment. We cannot therefore say whether the model is false or right, but we are still inside the error bars.

This is different for the two subsequent cases, i.e. the cases with a high Reynolds number, which have almost zero uncertainty but which above are superimposed on our Fluent results.

The results found are therefore satisfactory. In the following table, the same results, for the moments (N.m), are shown in percentage error.

	Case1	Case2	Case3	Case4
Fluent	0,2245	3,425	0,363	5,275
Miles	0,2975	3,385	0,43	5,162
Erreur %	-24%	1,2%	-15%	2,19%

Table 7 E% Miles'Cases

Therefore, it can be noticed that, leaving out case 1 and 3, that is the first two cases of image 57, the errors are very low. The accuracy is very good.

Let's now look at the velocity profiles, comparing them with Moghaddam's results. Case 1 and Case 2 are shown. For our post-processing we placed at the radii r*=0.62 and r*=0.80 (see Figure 58).

The figures 59-60 above shows also the k-ω SST model to finish our comparison between the two turbulence models regarding the profiles, as done in 4.1.3 and 4.2.2.

We have seen that, in the cases of Poncet and Coren, the k-ε realizable model was more consistent than the k-ω SST model, we can see in the figures above the same trend.
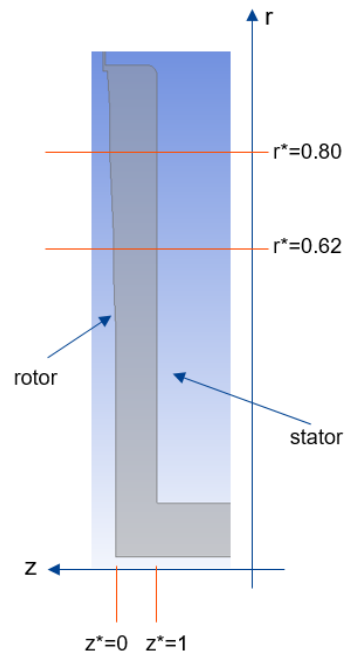
Figure 58 Post-processing r Miles*

For case 1, as in the case of Poncet and Coren, the two velocity profiles are very different. In general, the results of the realizable k-ε model are fairly consistent with Moghaddam's profiles.
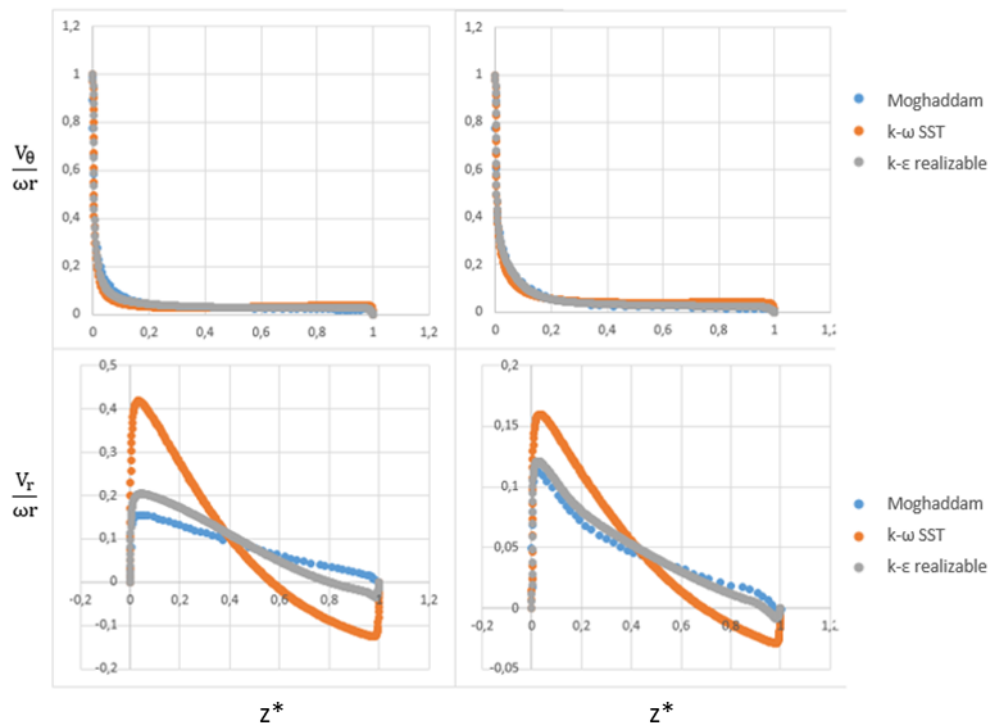
Figure 59 Radial and tangential velocity profiles, Miles Case1

57
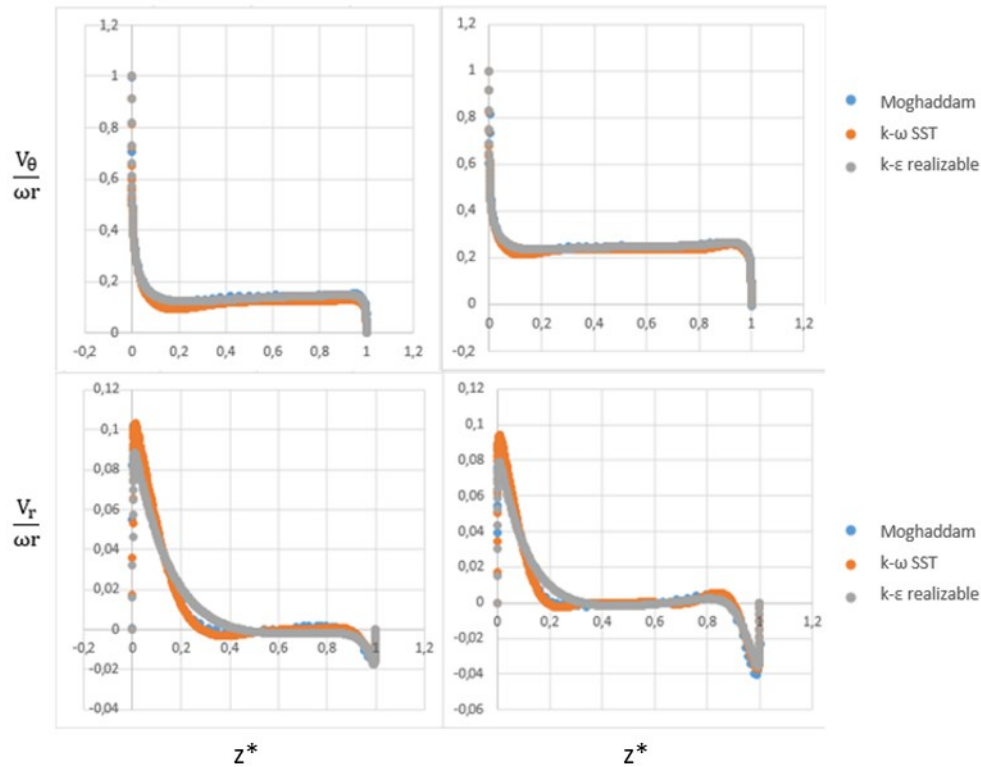
Figure 60 Radial and tangential velocity profiles, Miles Case2

For case 2, with high Reynolds, the two models always give similar results, as seen in 4.2.2. We can see how the k-ω model does not manage Stewartson-type flow very well, while it is in good agreement with Batchelor-type flow. For case 2, the results are almost entirely superimposed on the Moghaddam's results.

4.3 Errors in windage losses

In this paragraph we will show the errors of the windage losses both for Poncet and for the works of the University of Sussex.

As for the latter, the error is closely related to the error of the moment ($P[W] = M\omega$) so we can already give the error between the experimental works of Coren and Miles and the results obtained with our Fluent model:

- Coren's cases: $\varepsilon\% < 5\%$
- Miles' cases: $\varepsilon\% < 5\%$

The errors found are therefore satisfactory, both of which are less than 5%.

As for Poncet's thesis, due to the presence of results only concerning the radial and tangential velocity profiles, we cannot directly study the errors in power losses. We find the error using a correlation, since the τ_θ is not visible in our 2D model. The correlation is used with the radial profile of the tangential velocity. We then move on to the friction coefficient, on to the moment (Eq.7) to finish with the power losses, applied to experimental velocity measurements and CFD calculations.
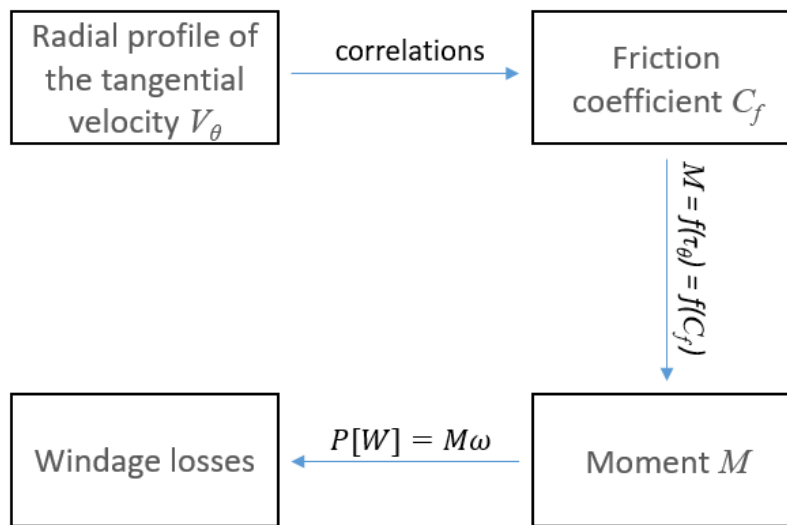
Figure 61 Strategy used to find windage losses with correlations

In this case, for the five centrifugal cases, the errors are as follows:

- Three centrifugal cases: $\varepsilon\% < 4\%$
- Two extreme cases: $\varepsilon\% < 1\%$

Also for the five centrifugal cases of Poncet, we find a good agreement with the experimental results, $\varepsilon\%$ is always under 5%.

For the centripetal case, we were not able to find satisfactory errors, although the velocity profiles were quite consistent with Poncet's experimental results.

In fact, the correlations depend on the coefficient C_f, which in turn also depends on the wall shear stress τ_θ. This means that a small initial error brings a great total error in the moment and therefore in the power losses (the errors merge). This happens in cases where K is large enough, as seen therefore for the centripetal case in which K was close to unity and could

also be 1,4. Still, we remind that for $K \approx 1$, the windage losses are minimized (low tangential stresses).

The following figures show how errors can in fact explode starting from a $K>0,5$ approximately. The curve was obtained using correlations, doing an influence study starting from the radial profile of K and getting the value $\varepsilon\%$ of the power losses. Figure 62 shows the error surface for a K ranging from 0.05 to 1,2 with an error ranging from -20% to +20%.
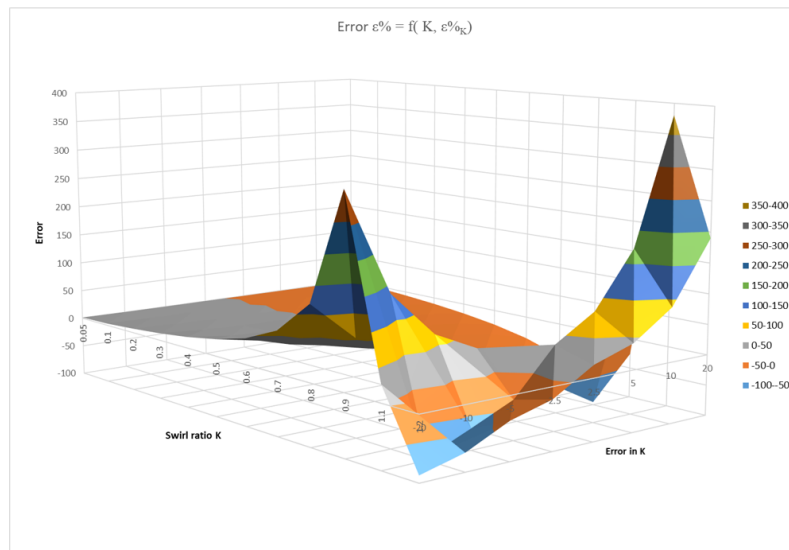
Figure 62 Error % as a function of K and ε%K

For greater clarity in the results, it has been divided into Figure 63 and Figure 64 which show the trend of errors for $K < 0,5$ and $K > 0.5$.
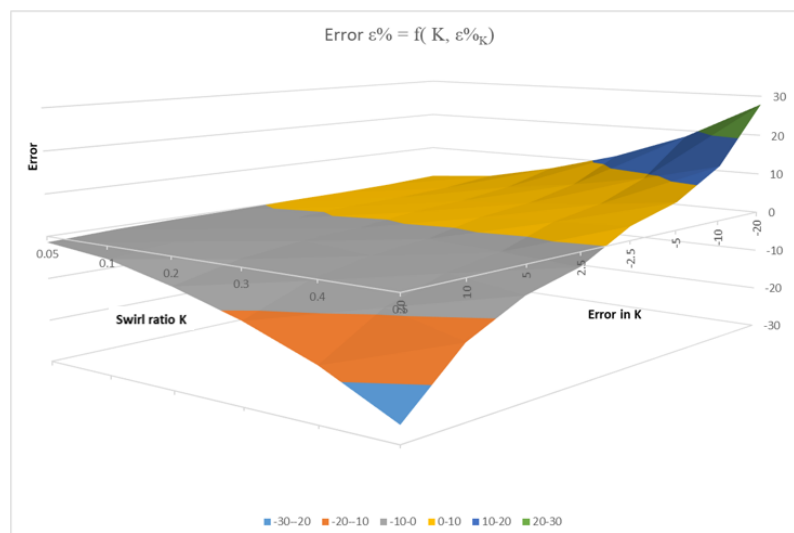
Figure 63 Error % as a function of K and ε%K, K<0.5

We can see how for a low *K* the error is relatively low and begin to rise when the error in *K* is high. If the swirl ratio is already high, on the other hand, we notice a large total error already with a small error in *K* (figure below).
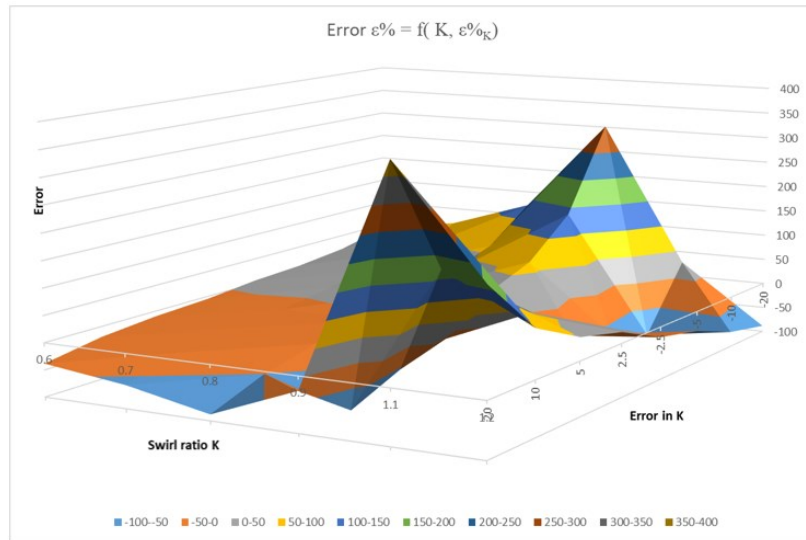
Figure 64 Error % as a function of K and ε%K, K>0.5

4.4 Conclusions

Thanks to the modelling of these academic test cases, we have been able to see that the results found are in excellent accord with the experimental works and that the k-ε realizable model has a greater coherence than the k-ω SST as regards the streamlines. For the DOE, therefore, the k-ε realizable model was chosen. It is, in our opinion, after the academic test cases, the best model to achieve a good result in terms of velocity profile, moment coefficient and stability (calculation time, computational cost and convergence).

5. Design of Experiments

In this chapter we will discuss the metamodeling theory and the Design Of Experiments (DOE). The focus will be on the definition of a DOE and on the choices best suited to our study case. The ANSYS software DesignXplorer offers different methods for defining a design of experiment, building the response surface and analyzing and post-processing the results.

5.1 Theory of Design of Experiments

Usually, DOE is used to see how different variables could affect a result. It is useful to find a good design point, which is often the result of a trade-off between various objectives [23]. During this "design exploration", we want to reach enough information about the current design to be able to answer "What-if" questions that quantify the influence of design variables on system performance. This way, we can make the right decisions based on accurate information and be sure of our analysis even in case of unexpected changes in the design constraints. Design exploration describes therefore the relationship between the design variables and the performance of the system using Design of Experiments (DOEs) and response surfaces. Once the variation of the system performance as a function of the design variables is known, we can understand and identify the changes required to meet requirements for our needs. We can analyze and share results using curves, surfaces, and sensitivities that are easily understandable.
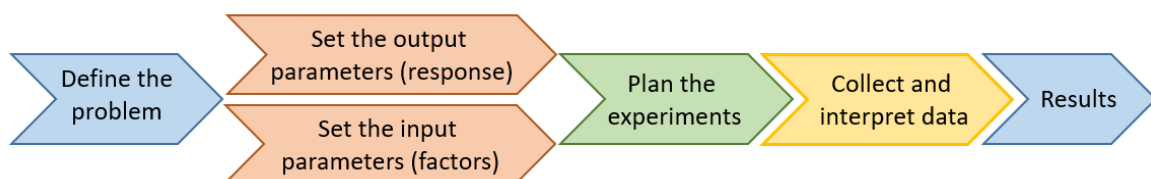
Figure 65 Design of Experiments – procedure

The first step of any design simulation is to create a model for the simulation [23]. The model can use a single physics or use multiple physics with many complex conditions. The second step is to define the design variables, the input parameters. They can include CAD parameters, loading conditions, material properties, and more. Then, we choose the output parameters, from the simulation results. In our case, we can use DesignXplorer, which provide tools to analyze a parametric design with a reasonable number of parameters.

Examples for a DOE are:

- Output parameters: maximum stress, mass, fluid flow, and velocities.
- Design variables: dimensions, loads, and material properties.

Once the initial model is created and the parameters defined, the next step is to create a response surface. The design space is defined by specifying the minimum and maximum values for each input variable. The Response Surface system depends on the selected DOE type.

DesignXplorer creates a response surface for each output parameter. A response surface is an approximation of the response of the system. Its accuracy depends on several factors, including complexity of the variations of the output parameters, number of points in the original DOE, and choice of the response surface type.

5.2 Ansys's DOE

Among the various options available in DesignXplorer, the most interesting choice for the definition of a DOE is the sampling technique called "Optimal Space Filling Design" (OSF). Briefly, OSF is a Latin Hypercube Sampling Design (LHS) that is enriched by post-processing. The LHS approach is a statistical method for generating a sample of parameter values from a multidimensional distribution. This sampling method is often used to construct numerical experiments or, for example, for Monte Carlo integration.

The method performs the sampling by ensuring that each sample is positioned in a space R of dimension m as the only sample in each hyperplane of dimension $m\text{-}1$ aligned to the coordinates that define its position. To better understand the idea behind this definition, in

the figure below, we give the example of a 4-element sample obtained with LHS for a space of dimension $m = 2$.
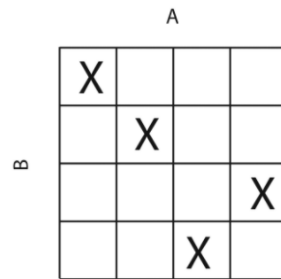
Figure 66 Exemple of LHS Sampling [22]

The OSF method is initialized as an LHS and then optimized several times, remaining a valid LHS (without points sharing rows or columns) while obtaining a more uniform spatial distribution of points (maximizing the distance between points).

OSF is able to distribute the design parameters uniformly throughout the design space with the objective of obtaining the best representativeness with the smallest number of points.
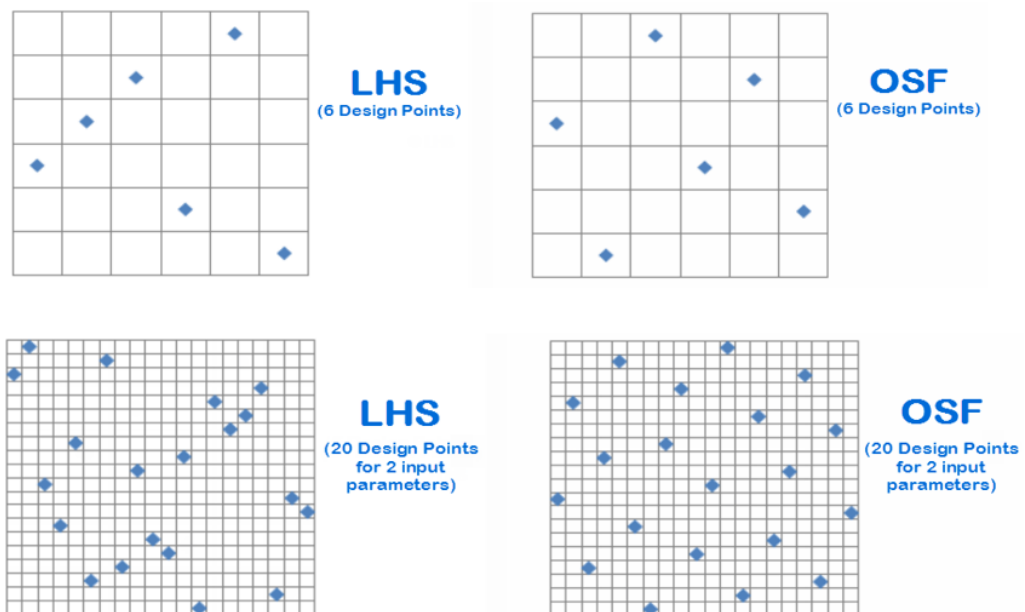
Figure 67 LHS vs OSF for 2 parameters and 20 design points [22]

This advantage makes it particularly interesting when a more complex meta-modeling technique such as *kriging*, *nonparametric regression* or *neural networks* are used [23]. It is interesting to further investigate the difference between LHS and OSF. Two comparisons of

sampled points are given in Figure 67, considering a search space of dimension 2 (2 design parameters) and respectively 6 and 20 sample points [23].

Since OSF incorporates the LHS algorithm, both types of DOE aim to conserve calculation resources by avoiding the creation of duplicate points. Given a sufficient number of design points, both methods can achieve high quality response prediction. However, the OSF algorithm has the additional advantage of a more complete coverage of the design space.

In a two-dimensional problem with two input parameters and six design points, it may be difficult to construct an adequate response surface, as we can see in the case of LHS due to the non-uniform distribution of design points in the design space (Figure 67, left). If we increase the number of design points for the same scenario to twenty, we notice that the quality of the resulting response surface is improved, both in the LHS and OSF method, but the LHS method can result in tight and irregular groupings of design points. This could be a problem due to the failure to take into account some parts of the design space. The OSF method, with its maximization of the distance between points and its more uniform distribution of points, handles the extremes more efficiently and covers the design space much better.

For this reason, the OSF method will be preferred for our DOE. In DesignXplorer, choices are available to adapt the OSF technique to the requirements of the problem we want to solve. In particular, there is the possibility to choose a certain "philosophy" in the generation of the sample and the number of points to be generated. Without reviewing the different options available, we will now detail the choices made in our study. In particular:

- The Maximum Entropy criterion was chosen for the sample generation, as it allows us to minimize the uncertainty in the unobserved regions of the space, which is important to ensure the desired accuracy
- The CCD Samples option was chosen for the determination of the number of points to be used in the DOE definition. The software will generate a sample with a number of points equal to that of a Central Composite Design (CCD) type DOE. This choice gives us the freedom to choose the meta-model to be used to interpolate the results a posteriori (i.e. after the simulation results). For any model chosen for data interpolation, the number of points of a CCD sample is able to give good results.

In general, to be able to launch a DOE, the ANSYS DX is used, which asks us to choose a minimum and maximum range between which to vary our parameters.
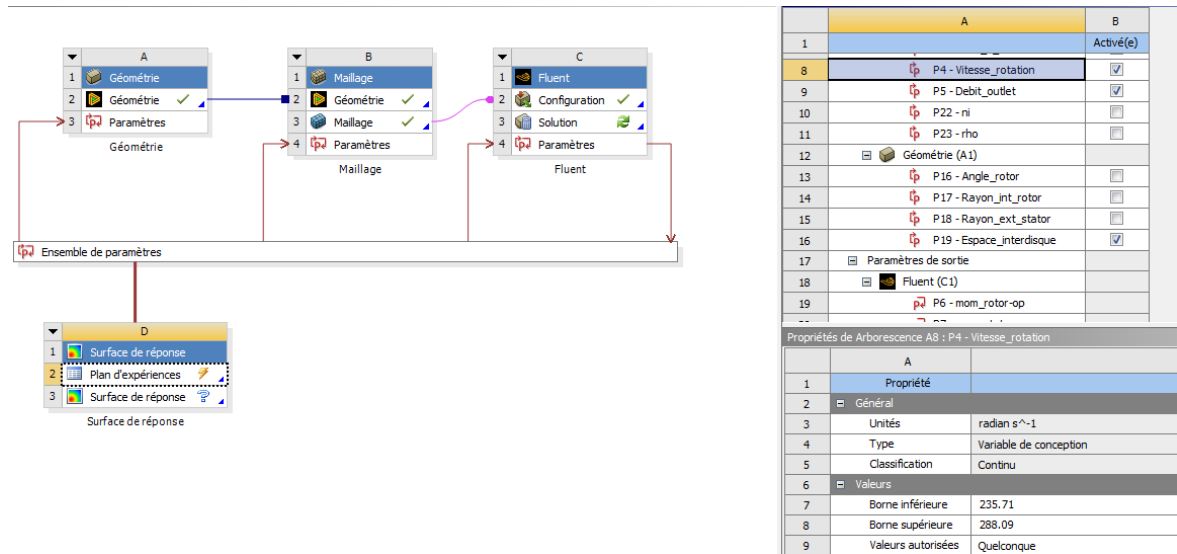
Figure 68 Example ANSYS DOE

In fact, it will be ANSYS who will choose, based on the inputs, the values in order to create the best possible response surface. In Figure 68 we can see ANSYS asking the "Borne inférieure/supériure", i.e. the minimum and maximum range of the value. Between these two "bornes" will be chosen all the values of the rotation speed to be used to launch the DOE.

In some cases, however, we may be interested in avoiding an automatic ANSYS DOE by launching a parametric calculation on Workbench. This could be an idea when some DOE inputs cannot be studied (and therefore must be studied separately) or if some design points of the DOE do not converge. In this last case, either they are removed from the DOE or they are studied separately, individually.

ANSYS gives us the possibility to choose, a bit like for the DOE, the inputs and outputs of our simulations, with the opportunity to change the inputs for each calculation point.

This means that it is therefore the user who chooses the values of the inputs and not ANSYS. As we can see in the right part of Figure 69 below, the calculation points are chosen by the user, which can be a variable number. ANSYS in this case starts the simulation starting from the first calculation point and, once the first point is completed, it moves on to the second and so on.

Figure 69 Example ANSYS parametric calculation

The outputs are chosen by the user and shown in the right column after the calculations (in our example mom_rotor).

After defining the DOE, the simulations are launched and the results obtained. ANSYS offers different ways to interpolate the results to finally obtain the response surface.

5.3 Response Surface

DesignXplorer, provides a tool for defining the response surface called *Genetic Aggregation* [23]. Genetic Aggregation automates the process of selecting, configuring and generating the most appropriate response surface type for each output of the problem under study. From the different types of response surfaces available (*full second order polynomial*, *nonparametric regression*, *kriging* and *least squares*), this method automatically builds the type of response surface that is the most appropriate approach for each output [23].

Nevertheless, Genetic aggregation is more time consuming than conventional response surfaces, due to multiple resolutions of the response surfaces and a cross-validation process, but in general, it is more reliable than conventional response surface meta-models.

It uses a fitness function, a special type of objective function that summarizes, in the form of a single figure of merit, how close a given design solution is to achieving its stated goals.

Fitness functions are used in genetic programming and genetic algorithms to guide simulations towards optimal design solutions.
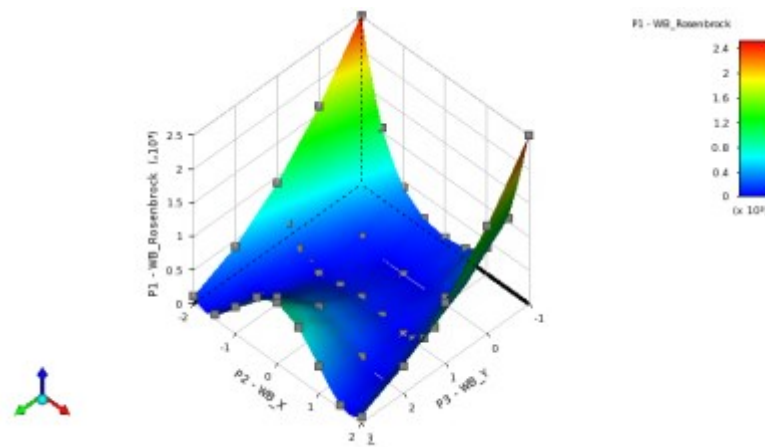
Figure 70 Response surface - Ansys [23]

It takes into account both the accuracy of the response surface on the design points and the stability of the response surface (cross validation). The response surface of genetic aggregation can be a single response surface or a combination of several different response surfaces (obtained by a crossover operation during the genetic algorithm) [23].

As the theory inherent in genetic aggregation is beyond the scope of this report, the reader is referred to the dedicated technical literature [23].

6. Launch of the First DOE

We can now continue with the first DOE. The first DOE incorporates a very simple rotor-stator cavity, with characteristics similar to the cavities studied in chapters 4. At the time this report was written (at about 4 months of internship), the first DOE was prepared, the first tests were performed to evaluate the strategy of convergence, the value of y^+ for different conditions and the computation time. The various options of the DOE have been examined (automatic and user-imposed). Therefore, the DOE was not launched, the results of which however could not have been shown due to the confidentiality of the subject.

6.1 Geometry and Parameters

The geometry is visible in the figure below. We therefore have a rotor wall, a stator wall and an axial flow inlet and outlet (as in the case of Poncet). Very generally, the figure also shows angles θ_1 and θ_2 as parameters:
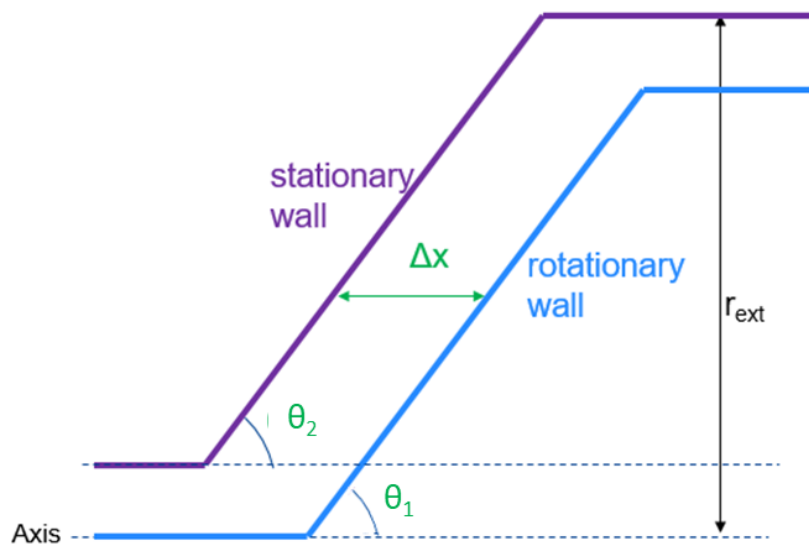
Figure 71 Rotor-stator cavity for the first DOE

<u>Windage Correlations for Flows in Rotor-Stator Cavities</u>

Since the geometry of a system can be very variable, some constraints have been placed on our DOE:

- No rotor/rotor or rotor counter-rotating cavities
- Angles tested $\theta = 45° - 90°$ with $\theta_1 = \theta_2$
- Cases with co-axial cylinders not yet treated

Before proceeding with the description of the DOE, it is necessary to study and define the values of the inputs and outputs to define. Today's engines, during their operating cycle (take-off, cruise, landing), have different values of Re_θ, C_w and λ_T.

Due to the confidentiality of these informations, these values will not be quoted into this report, but a qualitative comment will still be made, functional to the DOE.

In general, when an engine is running, these values can be quite different from each other. In the case of a DOE, it's not the best of situations. Only considering for example the range of the Rotational Reynolds number, it could vary by various orders of magnitude, but maybe only for some part of the engine. In these cases, throwing a DOE with covering the extreme values would not be correct, as ANSYS would create a too large surface of values and the simulations would take too long to give a solution. In this case, the best choice is to remove these extreme and singular points, work with a DOE in the average range of values and calculate each removed point individually. Furthermore, again for the different orders of magnitude, the idea is to divide the range into many small ranges and therefore launch smaller DOEs. At the time of writing this report, various tests have been carried out to understand whether it was better to choose to impose a DOE manually or automatically. In fact, the choice of the automatic DOE could lead to creating points of not too much interest and instead omitting important points.

On the other hand, however, a manual DOE means greater difficulty in choosing the points, in order to cover the whole range of variables for our needs. The choice fell on a manual DOE, which allows us to choose all the points of interest, based on the flight phases, aided by an automatic DOE.

For this first DOE, the outputs will be the moments on the surface of the rotor and the stator, the velocity profiles, temperature and pressure at inlet and outlet and the radial profiles of pressure P_s, P_t and temperature T_s, T_t. Furthermore, as shown in the following figure, the value of y^+ is shown for the rotor and the stator surfaces, so as to verify that it is always

below the value 3. We ask Fluent to calculate the y^+ for the surfaces, to take the max of it and show it as an output.

P14 - y-rotor-op	P15 - y-stator-op
0.88561	0.43486
1.6162	0.49205
2.0159	0.75415
2.6448	1.2242

Figure 72 y^+ for rotor and stator surfaces

6.2 Convergence strategy of DOE

In order to have an excellent convergence, and to be sure that this happens, a strategy has been defined for Fluent in our DOE. This strategy is the same used also in the previous chapters for the academic test cases.

Generally speaking, the simulations will be performed in *pseudo-transient*, a method that is an accelerated solver for getting the steady state solution much faster than the classic *CFL* method, but still linked to it.

$$CFL = CFL_{ref} * TSF \tag{28}$$

where $CFL_{ref} = 200$ and TSF is the Time Scale Factor.

If the pseudo-transient is not selected for the calculation, it is in the Solution Controls tab that the number of *CFL* is controlled. This number represents the ratio of distance travelled by a fluid particle in a time step to the size of the mesh, i.e.:

$$CFL = \frac{v\,\Delta t}{\Delta x} \tag{29}$$

Where v is the speed of the fluid particle, Δt the time step (for a stationary calculation, it is in fact the transition from one iteration to another) and Δx the characteristic size of the mesh.

This number represents the speed at which information travels through the domain. Fluent being an implicit code, the number of CFL can vary between 1 and several hundreds. The higher the CFL, the faster the solution converges but the less stable the calculation. At the

start of the calculation, it may therefore be interesting to reduce the *CFL* to stabilize the calculation and then increase it gradually.

With a pseudo-transient method, our strategy for our DOE is therefore the following:

- 50 iterations with *TSF* = 0.005
- 50 iterations with *TSF* = 0.01
- 50 iterations with *TSF* = 0.025
- 50 iterations with *TSF* = 0.05
- 250 iterations with *TSF* = 0.1
- 250 iterations with *TSF* = 0.25
- 4250 iterations with *TSF* = 0.5

The iterations at *TSF*=0.5 are fixed in a generic way, there will be convergence conditions.

The iterations are so quite high in order to join always these conditions before the end of the simulations:

- For Residuals: 10^{-4}
- For Energy Residuals: 10^{-6}

Furthermore, another check for the convergence will be the variation of Monitors reports. We choose a variation less than 0.0001 (so 0.01 %) to observe after 500 iterations and every 50 iterations. If our simulation joins all these conditions, the solution can be defined converged.

Figure 73 below shows an example of the convergence of a solution. If the residuals are converged, Fluent continues to evaluate the Monitor Reports to join the condition of 0.01% every 50 iterations. As one monitor converges, Fluent prints "Solution for report definition *ReportName* has converged" and when all the monitors are converged, the calculation stops. After that, we can ask Fluent to post-process some results. In our DOE in fact, we are not able to do a post-processing for every design point, it would be too much expensive in terms of time. So, we have to write some TUI (Terminal User Interface) commands in the Calculation Activities in order to have the outputs, the files and the graphics desired.

Always in the Figure 73, for example, we created and wrote in a file an XY plot with a TUI command, we asked for the radial profile of the static temperature along all the cavity (modification 9).

74

```
Solution for report definition report-def-0 has converged
Solution for report definition report-def-0-1 has converged
Solution for report definition report-def-0-1-1 has converged
Solution for report definition report-def-0-1-1-1 has converged
Solution for report definition report-def-1 has converged
Solution for report definition report-def-1-1 has converged
Solution for report definition report-def-2 has converged
Solution for report definition report-def-2-1 has converged
! 2950 report definition solution is converged
  2950  3.0498e-05  4.1316e-08  3.3289e-08  1.6716e-09  2.3472e-10  6.7469e-08  1.0334e-07  0:54:05 2000
! 2950 solution is converged
Executing Modification 9...
plot/plot y Temp y n n temperature n n radial-coordinate line05 ()

>

  iter  continuity  x-velocity  y-velocity      swirl      energy         k    epsilon    time/iter
  2950  3.0498e-05  4.1316e-08  3.3289e-08  1.6716e-09  2.3472e-10  6.7469e-08  1.0334e-07  0:00:00    0
! 2950 solution is converged
```

Figure 73 Converged solution example Fluent

The solver chosen is the Pressure-Based Coupled solver. It is suitable for all subsonic applications or applications with a Mach number lower than 2 and in which acoustics is not a phenomenon of interest. It is more accurate and valid over a higher range of calculations than the Pressure-Based Segregated (or Simple) solver. However, it does not solve acoustics or flows with a very high Mach number, flows for which a Density-Based solver would be more suitable. Since this type of problem is not encountered in this work, the use of the Pressure-Based Coupled solver was chosen.

Figure 74 Solution Method Fluent

75

Regarding the Spatial Discretization, the Gradient will be Green-Gauss Node Based. In general, we can choose between:

- Green-Gauss Cell Based
- Green-Gauss Node Based
- Least Squares Cell Based

The Green-Gauss Node Based is based on the Green-Gauss Theorem. It is more precise than the others and it has the advantage of minimizing digital diffusion, it can be used when the mesh is irregular and unstructured, however, its computational cost is higher.

The other Solution Methods for the Spatial Discretization are the Second Order Upwind and PRESTO! for Pressure, usually used when the fluid is in rotation (swirl).

For our simulations, the characteristics of the air will be used. Once the results are obtained through the DOE, they will be compared with the correlations used by Safran Aircraft Engines, in order to confirm and possibly increase the validity domain of these correlations.

6.3 DOE tests and results

Before starting the real DOE, some tests were carried out in order to be sure about the stability and the convergence of the simulation. Moreover, other tests about the geometry were included to evaluate the differences, if present, in changing the area of the inlet and the distance of the rotor surface from the axis.

Several geometries have been tested in order to verify that the flow and moment are influenced only by the dimensionless numbers Re_θ et C_w.

The next figure shows two different geometries:

- 1st geometry: inlet on the axis
- 2nd geometry: 25mm distance from the axis

A third geometry was tested with 15mm distance from the axis, not shown in the figure.
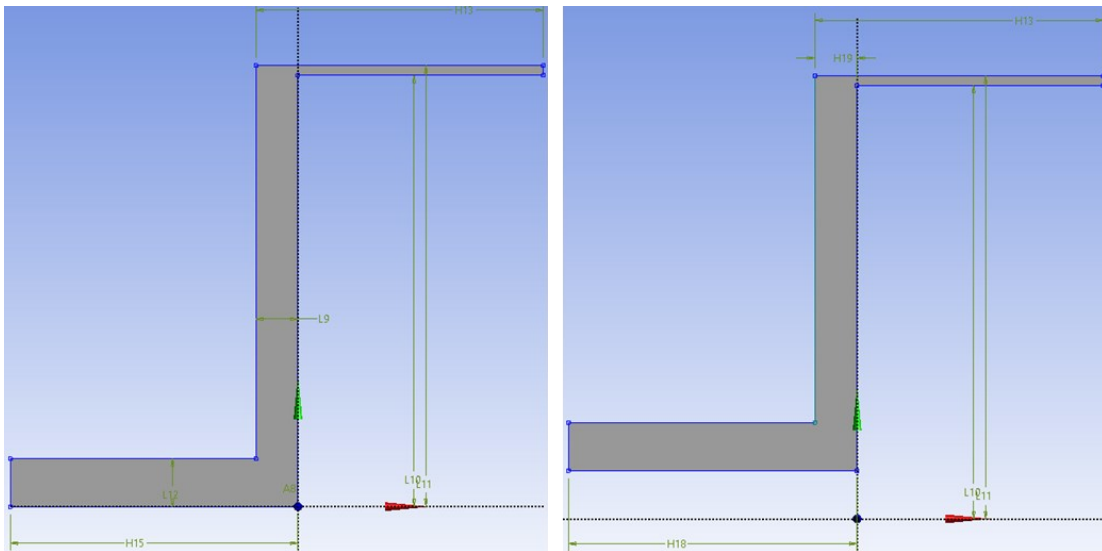
Figure 75 DOE tests: influence in geometry

For all these geometries, the radius b was always the same, b=225mm, in order to have the same Re_θ et C_w (keeping the same flow rate and rotation velocity).

The following table shows the results regarding the moment on the rotor surface for these different configurations:

Moment rotor [N.m]	Configuration 1	Configuration 2	Configuration 3
Cas1	0.465	0.461	0.465
Cas2	1.146	1.141	1.146
Cas3	1.960	1.956	1.959
Cas4	2.743	2.742	2.743

Table 8 Moment on the rotor for different geometries

As we can notice, the results are almost the same, which confirm thus the dependence only on the dimensionless parameters.

The goal of the internship was to verify the validity range of some correlations, using a Fluent model created specifically to be able to build and launch different Design of Experiments. Through other DOEs, an attempt was also made to extend the validity range of the correlations, thus increasing some parameters, which were not initially foreseen, and changing the geometries in order to simulate the real dimensions of rotor-stator cavities of SAE engines.

Windage Correlations for Flows in Rotor-Stator Cavities

The following figure shows, qualitatively, a cartography representing the coherence between the correlations and the Fluent model. Unfortunately, due to the confidentiality of these correlations and data, the real values of the results cannot be shown.
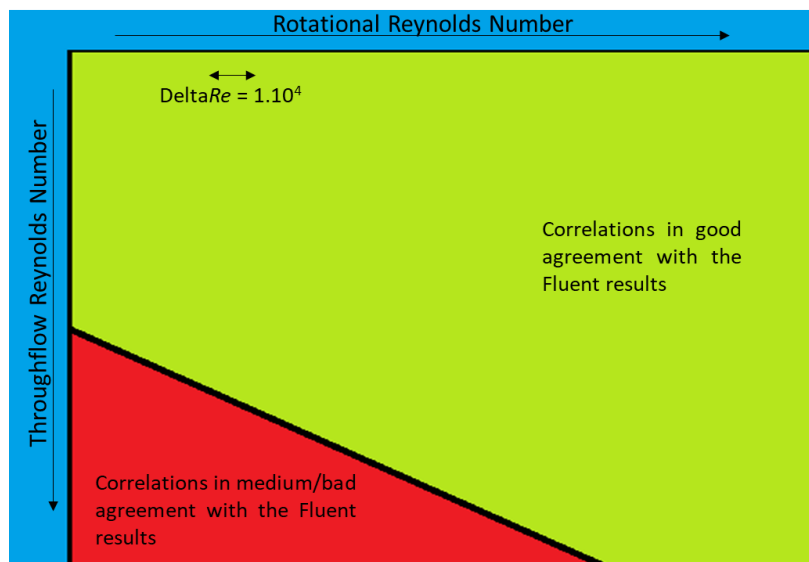
Figure 76 Coherence Correlations/Fluent

In the abscissas we have the Reynolds rotational number, while in the ordinates we have the Throughflow Reynolds number, which, as we recall, form the turbulence parameter λ_T according to the formula $\frac{C_w}{Re_\theta^{0.8}}$.

We can see from the cartography, how, first of all, the range of valid values (green) is much larger than the range of invalid values (red). This shows thus a good coherence between correlations and our Fluent model. Furthermore, this red range is located in an area with low Re_θ and high C_w, therefore with a high turbulence parameter. The green range, on the other hand, is located in areas with either a high Reynolds number or a low C_w, i.e. in general with a medium-low turbulence parameter.

One thing that can therefore be stated is that a high turbulence parameter can affect the accuracy of the results, while with a low average turbulence parameter, the results of correlations have a very low error in comparison with the Fluent results.

7. Conclusions and Perspectives

With this thesis we wanted to show the methodology, some results and studies concerning the rotor-stator cavities in aircraft engines.

These systems are of fundamental importance, for example, for the cooling of turbines. The losses generated must therefore be as small as possible, remembering that every loss in the engine means less efficiency and performance degradation.

We were therefore able to see a bibliographic overview for this type of systems, the validation of a Fluent model thanks to the comparison with some experimental works and the methodology used to launch some design of experiments, which will allow us to evaluate the error in the correlations used by SAE.

Due to the confidentiality of this stage, not all data and results were fully described regarding the DOE, but at least a qualitative description of the strategy and some results has been provided.

The prospect of this internship is therefore to continue to launch DOEs and possibly improve the validity domain of the correlations already used in the company.

During the period of internship at Safran Aircraft Engines, I had the opportunity to work in a team with experienced engineers, who have been working in this field for years. I was able to question my knowledge and skills, a path that has certainly formed and improved me in a professional (and human) point of view.

Appendices

Appendix 1: Laser Doppler Anemometry

Laser Doppler Anemometry (LDA) was used to measure radial and tangential components of the air velocities in the rotor-stator cavity in the studied theses (Coren and Poncet). As it has therefore been mentioned, it seemed right to make a small summary of that.

When light is reflected from a moving object, the frequency of the scattered light is shifted by an amount proportional to the speed of the object. So, the speed could be estimate by observing the frequency shift. This is the basis for LDA [24]. A flow is seeded with particles that scatter light. The particles are illuminated by a known frequency of laser light. The scattered light is detected by a photomultiplier tube (PMT), an instrument that generates a current in proportion to absorbed photon energy, and then amplifies that current. The difference between the incident and scattered light frequencies is called the Doppler shift.
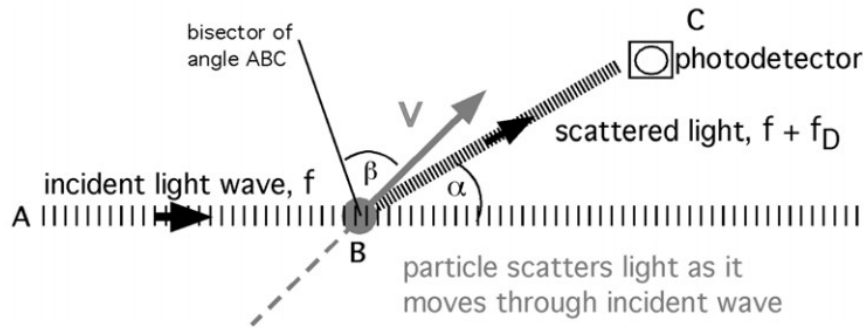
Figure 77 Laser Doppler Anemometry

The Doppler shift, f_D, depends on the speed, V, and direction of the particle motion, the wavelength of the light, λ, and the orientation of the observer. The orientation of the observer is defined by the angle α between the incident light wave and the photodetector [PMT]. The direction of particle motion is defined by β. The Doppler shift is defined as following:

$$f_D = \frac{2V}{\lambda} cos\beta \ sin\frac{\alpha}{2} \tag{30}$$

A direct way to estimate f_D is to measure the incident frequency, f, and the observed frequency, f_O, and find the difference. However, the Doppler shift is a very small fraction of the incident frequency, this results in estimating a small value from the difference of two large values, a process with a high degree of uncertainty. To improve the estimate of f_D, a method using two incident beams has been developed. In this configuration the incident beam is split into two beams of equal intensity [24]. The beams are directed to intersect, and the point of intersection is the measurement volume. Particles that pass through the measurement volume scatter light from both beams. The frequency shift of the light scattered from each beam will be different, because the orientation of the two beams relative to the photodetector and relative to the particle's velocity vector are different.
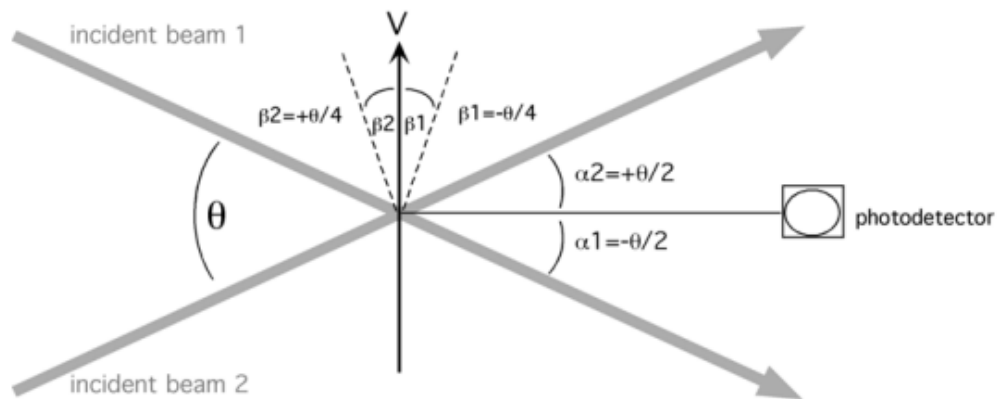
Figure 78 Differential Laser Doppler Anemometry

Another useful way to interpret the signal recorded by the photodetector is in terms of the interference fringe pattern generated at the beam crossing. The fringe pattern, consists of alternating zones of brightness and darkness. As a particle crosses the fringe pattern, the intensity of the scattered light varies with the intensity of the fringes. The photodetector records a signal burst whose amplitude is modulated by the fringe pattern.

In the case of Poncet's work, for example, two laser sources each emit coherent light separated into two beams: a source emitting a pair of green beam and a source emitting two beams of red color. These pairs of beams make it possible to obtain two components of the speed.

Appendix 2: Y plus

Turbulent flows in CFD (Computational Fluid Dynamics) are significantly affected by the presence of walls, where the viscosity-affected regions have large gradients in the solution variables. An accurate representation of the near wall region determines a successful prediction of wall bounded turbulent flows. As the velocity profile is quite "general", functions can be applied to determine the quantities at the wall: these functions are called "wall law". At the wall, the gradients are important and the precise resolution of the wall is required to obtain a realistic simulation. Two approaches are possible [25]:

One way is to integrate the turbulence to the wall, another way is to use the so-called wall functions. One of the most prominent parameters when judging the applicability of wall functions is the so-called dimensionless wall distance y^+:

$$y^+ = \frac{u^* y}{\nu} \tag{31}$$

Where u^* is the friction velocity at the nearest wall, y is the distance to the nearest wall and ν is the local kinematic viscosity of the fluid. One can interpret y^+ as a local Reynolds number, which means that its magnitude can be expected to determine the relative importance of viscous and turbulent processes.

In general, we can define three layers [26], Figure 77:

- The viscous sublayer ($y^+ < 5$):
  In the viscous layer, the fluid is dominated by the viscous effect, so it can be assumed that the Reynolds shear stress is negligible. The "linear velocity law" is given by:
  $$y^+ = u^+ \tag{32}$$

- The logarithmic area ($y^+ > 30$):
  In the logarithmic layer, turbulence stress dominate the flow and velocity profile varies very slowly with a logarithmic function along the distance y.

The formula below describes this region with the Karman constant κ of 0.41 and the constant B=5.2.

$$u^+ = \frac{1}{\kappa}\ln(y^+) + B \tag{33}$$

- The Buffer layer ($5 < y^+ < 30$)

  The buffer layer is the transition region between the viscosity-dominated region and turbulence-dominated part of the flow. Viscous and turbulent stresses are of similar magnitude and since it is complex, the velocity profile is not well defined and the original wall functions avoid the first cell located in this region.
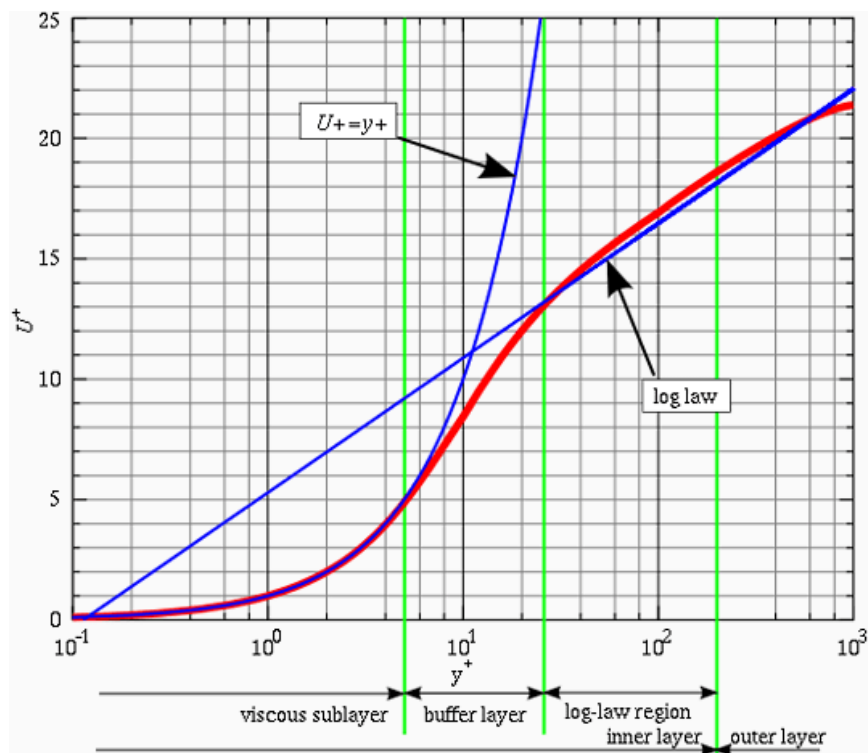
Figure 79 The wall law and velocity profile in the boundary layer [25]

If we want to integrate the turbulence to the wall, turbulence models are modified to enable the viscosity-affected region to be resolved with all the mesh down to the wall, including the viscous sublayer. In order to resolve the viscous sublayer, the first cell must be placed in this viscous sublayer ($y^+ < 3$ for aerodynamic problems) leading to the requirement of abundant mesh cells (Figure 78). Thus, substantial computational resources are required.
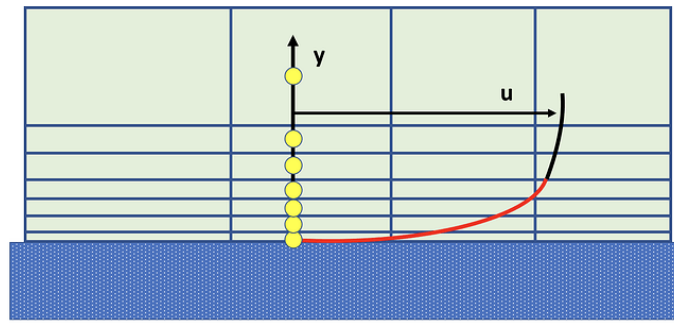
Figure 80 Viscous Sublayer (red) and mesh discretisation (yellow circle)

Then, we could use the wall functions, which can model the near wall region. Wall functions are equations empirically derived and used to satisfy the physics in the near wall region. The first cell needs to be placed in the log-law region to ensure the accuracy of the results (Figure 79). Wall functions are used to bridge the inner region between the wall and the turbulence fully developed region. When using the wall functions approach, there is no need to resolve the boundary layer causing a significant reduction of the mesh size and the computational domain. The first grid cell needs to satisfy $30 < y^+ < 300$ (if this is too low, the model is invalid. If this is too high, the wall is not properly resolved). It is used when you are more interested in the mixing rather than the forces on the wall.

Figure 81 Mesh discretisation relevant for wall functions

<u>Appendix 3: Turbulence Models</u>

The different turbulent flows have many peculiar characteristics:

- They can be 3D (homogeneous and isotropic turbulence, internal flows, ...) or almost 2D (atmospheric fluxes, conductive fluxes in the presence of magnetic fields very intense and stably oriented, ...)
- Presence of persistent coherent structures on average (bubbles of recirculation, secondary motions in square section channels, ...) or not (homogeneous and isotropic turbulence, parallel plane channel, flow in circular section ducts, ...)
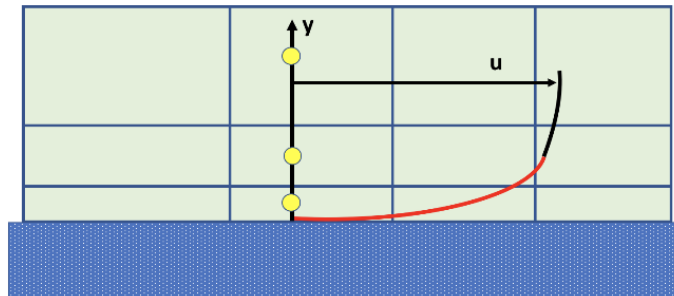- Transitional flows

Therefore, it is difficult to characterize a turbulent flow. Intuitively, turbulent flow is characterized by disorder in space and time. Turbulent flows are non-stationary and chaotic, with a huge range of spatial and temporal scales, so one approach completely statistical neglects the existence of coherent structures, repeatable and deterministic events, responsible for most of the turbulence effects.

It is therefore particularly difficult to develop a procedure calculation/model to produce accurate previsions for all situations of practical interest and at an acceptable cost. Turbulent flows can be simulated by DNS, LES and RANS models [26].

In DNS (Direct Numerical Simulation) models the Navier-Stokes equations are solved numerically in their non-stationary three-dimensional formulation. The advantages of the DNS approach are the absence of empirical models and parameterizations, the quality and quantity of information (statistical quantities) otherwise unavailable. But, because of that, it is extremely computationally expensive (non-stationary 3D simulation) with tens or more often hundreds/thousands of CPU hours. So, it is limited to simple geometries, to weakly turbulent flows and low values of the number of Reynolds.

Another approach can be the LES. The basic idea of the LES approach is based on experimental observations that the turbulent structures of greater size constitute the most

significant energy contribution (energy-containing eddies) and therefore are responsible for most of the effects while the smallest (dissipative) structures are essentially isotropic and universal, that is, they do not depend on the specific problem (geometry etc.).

Therefore, it seems logical to use a numerical approach that captures directly, through a non-stationary 3D simulation, the spatial scales of greater dimension (Large Eddies), delegating to an appropriate model the effects of smaller scales. This approach is still expensive, although less expensive, theoretically, than DNS.

In general, for a lot of engineering studies, the RANS equations are used. The interest of RANS (Reynolds Averaged Navier-Stokes equations) models is related to average values of the quantities as friction coefficient, coefficient of heat exchange and average course of the flow field. For this reason, the RANS method is better than the methods seen above, DNS and LES, compared to the usual needs. It is a method which, at acceptable cost, provides results of immediate practical interest, a model based on average quantities, where average means time average.

The averaging operation is performed on an infinite interval, for stationary flows, or over a large but finite interval for non-stationary flows (ensemble averaging). Each characteristic quantity of turbulent motion φ is decomposed into a term averaged over time and in a disturbance or fluctuation φ':

$$\varphi = \bar{\varphi} + \varphi' \tag{34}$$

According to Boussinesq's hypothesis, Reynolds' turbulent efforts can be assimilated to the effects of an additional viscosity, which varies from point to point, called turbulent viscosity μ_t:

$$-\rho u'_i u'_j = \mu_t \left(\frac{\partial \bar{u_i}}{\partial x_j} + \frac{\partial \bar{u_j}}{\partial x_i} \right) \tag{35}$$

which, inserted in the equation of momentum, provides:

$$-\rho \frac{\partial \bar{u}}{\partial t} + \rho \bar{u} \cdot \nabla \bar{u} + \nabla \bar{p} - (\mu + \mu_t)\nabla^2 \bar{u} + \rho \bar{F_m} = \mu_t \left(\frac{\partial \bar{u_i}}{\partial x_j} + \frac{\partial \bar{u_j}}{\partial x_i} \right) = 0 \tag{36}$$

In one of the simplest approach, turbulence is characterized by two parameters: a length scale L, and turbulent kinetic energy, k where k is:

$$\text{Appendices}$$

$$k = \frac{1}{2}u'_i u'_i \tag{37}$$

Based on the dimensional analysis, it can be shown that:

$$\mu_t = C_\mu \rho q L \tag{38}$$

where q is the velocity $q = (2k)^{1/2}$ (39)

Again, on the basis of dimensional analysis, and with the hypothesis of production e perfectly balanced turbulent kinetic energy dissipation (equilibrium turbulent flows), we have:

$$L \approx \frac{k^{\frac{3}{2}}}{\varepsilon} \tag{40}$$

Where is the dissipation of turbulent kinetic energy, $\varepsilon = \nu \frac{\partial u'_i}{\partial x_k}\frac{\partial u'_i}{\partial x_k}$ (41)

Given the need to have two quantities, speed and length scale, it seems natural to adopt a two-equation model. The RANS simulations depend different things and especially on the turbulence model; it is necessary to choose the good model choice as well as to provide a suitable numerical grid for the selected model.

The choice of turbulence model will depend on considerations such as the physics of the flow, the established practice for a specific class of problem, the level of accuracy required, the available computational resources, and the amount of time available for the simulation.

Below we will describe the two models used in our work, the RSM model, used by Poncet, and the Spalart-Allmaras model (described because quite used in Fluent but not in this internship).

Spalart-Allmaras

Spalart-Allmaras is a single transport equation model. It is designed for aerospace applications and involves wall-bounded flows on a fine near-wall mesh. In order to predict vertical flows, the strain rate in k production can be included. However, it is not good enough for 3D flows and flows with strong separation. It is very good for simulating airflows, fuselages, missiles.

K-ε Models

The k-ε model is a two-equation model, historically the most widely used turbulence models in industrial CFD. It solves two transport equations and model the Reynolds Stresses using the Eddy Viscosity approach. There are different k- ε models, the most used are:

- The Standard k-ε model, the most used model in practical engineering flow calculations. Robustness, economy, and reasonable accuracy for a wide range of turbulent flows explain its popularity in industrial flow and heat transfer simulations. The model is therefore not widely recommended in external aerodynamics. It performs poorly for complex flows (severe pressure gradient, separation).

- The Realizable k-ε model, recommended because it accurately provides superior performance for flows involving rotation, boundary layers under strong adverse pressure gradients, separation and recirculation [23]. It derives from the standard k-ε model with "realizable" changes to improve his performance.

K-ω Models

In k-ω models, the transport equation for the turbulent dissipation rate ε, is replaced with an equation for the specific dissipation rate ω. The ω-equation (two equations model too) offers several advantages relative to the ε-equation. The most prominent one is that the equation can be integrated without additional terms through the viscous sublayer. Also in this case, we have different k-ω models:

- The standard k-ω model, a model with good performances for wall-bounded boundary layers, free shear and low Reynolds number flows. However, it is not generally recommended because of his excessive and early prediction of separation.

- The SST k-ω models, designed to avoid the freestream sensitivity of the standard k-ω model. The SST model is a hybrid two equation model that combines the advantages of k-ε and k-ω models. Furthermore, these models are typically better at predicting separation, transition, low Re effects and impingement. Depending on wall distance makes it is less suitable for free shear flows.

Appendices

RSM Models

The Reynolds Stress Models (RSM) or Reynolds Stress Transport Models, represent the most complete classical turbulence models. The method of closure is the so-called Second Order Closure [26]. The most importance difference in this model is that in Reynolds Stress Models, the eddy viscosity approach is avoided and the individual components of the Reynolds stress tensor are directly computed. This means that five additional transport equations are required in 2D flows, in comparison to seven additional transport equations solved in 3D [23]. Its fidelity is limited by the closure assumptions in the transport equations for the Reynolds stresses, for example, the modelling of the pressure-strain and dissipation-rate terms is particularly difficult, and often considered to be responsible for compromising the accuracy of RSM predictions. However, the model has really good predictions for complex flows, streamline curvature, swirl and rotation, but it requires more CPU time and memory.

To sum up these models, below is a summary of the most common uses ANSYS recommendations [23]:

- With $y^+ > 30$ the Realizable k-ε model is recommended
- With $y^+ < 3$ the Realizable k-ε model with Enhanced Wall Treatment or the SST k-ω model
- For external aero applications: SST k-ω model ($y^+ < 3$)
- For internal aero applications: Realizable k-ε model with Enhanced Wall Treatment is recommended for convergence reasons.

References

[1] Rolls-Royce, 1986, *The Jet Engine*

[2] Ekman, 1905, *On the influence of the Earth's rotation on ocean currents.*

[3] Von Karman. *Uber laminare und turbulente Reibung.*

[4] Coren, 2007, *Windage due to Protrusions in Rotor-Stator Systems*, PhD Thesis

[5] Bodewadt, 1940, *Die Drehströmug über Festem Grunde*

[6] Batchelor, 1950, *Notes on a Class of Solutions of the Navier-Stokes Equations Representing Steady Rotationally Symmetric Flow*

[7] Stewartson, 1952, *On the Flow between Two Rotating Coaxial Discs*

[8] Daily, Nece, *Chamber Dimension Effects on Induced flow and Frictional Resistance of Enclosed Rotating Disks*

[9] Owen, 1969, *Flow Between a Rotating and a Stationary Disc*

[10] Owen, 1989, *An approximate Solution for the flow between a Rotating and a Stationary disk*

[11] Poncet, 2005, *Ecoulements de type rotor-stator soumis à un flux axial: de Batchelor à Stewartson.* Université de Provence, PhD Thesis

[12] Gartner, 1997, *A Prediction Method for the Frictional Torque of a Rotating Disk in a Stationary Housing with Superimposed Radial Outflow*

[13] Miles, 2011, *An Experimental Study of Windage due to Rotating and Static Bolts in an Enclosed Rotor-Stator System,* PhD Thesis

[14] Moghaddam, 2014, *Numerical Investigation of Fluid Flow in Protruded Rotor-Stator Cavities*, PhD Thesis

[15] Saari, *Thermal Analysis of High-speed Induction Machines*

[16] Gazley, 1958, *Heat transfer characteristics of the rotational and axial flow between concentric cylinders*

[17] Yamada, 1962, *Torque Resistance of a Flow between Rotating co-Axial Cylinders Having Axial Flow*

[18] Yamada, 1962, *Resistance of a Flow through an Annulus with an Inner Rotating Cylinder*

[19] Bilgen, 1973, *Functional Dependence of Torque Coefficient of Coaxial Cylinders on Gap Width and Reynolds Numbers*

[20] Poncet, 2010, *Numerical modelling of fluid flow and heat transfer in a narrow Taylor-Couette-Poiseuille system*

[21] Schreck, 2018, *Optimisation de la modélisation thermique de turbines haute pression par utilisation de calculs CFD*, Safran Aircraft Engines

[22] Millward, Edwards, 1994, *Windage Heating of Air Passing Through Labyrinth Seals*

[23] Ansys Help and Manuals V21

[24] Durst, Melling, Whitelaw, 1981, *Principles and Practices of Laser Doppler Anemometry*

[25] www.simscale.com

[26] Calmet, *MTURB Courses*, Ecole Centrale de Nantes